MASARYKOVA UNIVERZITA
PŘÍRODOVĚDECKÁ FAKULTA
ÚSTAV TEORETICKÉ FYZIKY A ASTROFYZIKY

Bakalářská práce

BRNO 2026 TERÉZIA DEBNÁROVÁ

MASARYKOVA
UNIVERZITA
PŘÍRODOVĚDECKÁ FAKULTA
ÚSTAV TEORETICKÉ FYZIKY A ASTROFYZIKY

Struktury radiového kontinua u blízkých galaktických medúz

Bakalářská práce

Terézia Debnárová

Vedoucí práce: Mgr. Pavel Jáchym, Ph.D. **Brno 2026**

Bibliografický záznam

Autor:	Terézia Debnárová Přírodovědecká fakulta, Masarykova univerzita Ústav teoretické fyziky a astrofyziky
Název práce:	Struktury radiového kontinua u blízkých galaktických medúz
Studijní program:	Fyzika
Studijní obor:	Astrofyzika
Vedoucí práce:	Mgr. Pavel Jáchym, Ph.D.
Akademický rok:	2025/2026
Počet stran:	xvii + 44
Klíčová slova:	Medúzovité galaxie; interferometr LOFAR; galaktická kupa Coma; evoluce galaxií; morfologie galaxií

Bibliographic Entry

Author:	Terézia Debnárová Faculty of Science, Masaryk University Department of Theoretical Physics and Astrophysics
Title of Thesis:	Radio continuum structures in nearby jellyfish galaxies
Degree Programme:	Physics
Field of Study:	Astrophysics
Supervisor:	Mgr. Pavel Jáchym, Ph.D.
Academic Year:	2025/2026
Number of Pages:	xvii + 44
Keywords:	Jellyfish galaxies; LOFAR interferometer; Coma galaxy cluster; galaxy evolution; galaxy morphology

Abstrakt

V této práci se zabýváme základními vlastnostmi rádiového kontinua jellyfish galaxií v galaktické kupě Coma. Tyto galaxie jsou ovlivňovány dynamickým tlakem horkého mezigalaktického plynu, který z nich odstraňuje mezihvězdný plyn, kosmické záření i magnetická pole a vytváří charakteristické „kometární“ ohony. Rádiové kontinuum odpovídá synchrotronnímu záření relativistických elektronů vznikajících zejména při explozích supernov. Pomocí analýzy dat z projektu LoTSS observatoře LOFAR zkoumáme přítomnost rádiového kontinua a morfologii těchto galaxií. Využíváme metody analýzy obrazových dat a statistického zpracování, zejména měření lokální úrovně šumu a tvorbu konturových map oddělujících skutečný signál od šumu. Šest jellyfish galaxií nebylo v datech LOFAR detekováno, zatímco u vybraných detekovaných galaxií podrobně popisujeme jejich rádiovou morfologii. Analyzujeme také změnu šířky rádiových ohonů se vzdáleností od středu galaxie a porovnáváme vlastnosti galaxií v rádiovém kontinuu a v Hα záření, které mapuje ionizovaný plyn. Pozorujeme přibližně lineární závislost mezi tokem Hα záření a celkovým rádiovým tokem, kvalitativně odpovídající známému vztahu mezi rádiovou luminozitou a rychlostí tvorby hvězd ve spirálních galaxiích.

Abstract

In this thesis, we investigate the basic properties of the radio continuum emission of jellyfish galaxies in the Coma Cluster. These galaxies are affected by the ram pressure exerted by the hot intracluster medium, which removes interstellar gas, cosmic rays, and magnetic fields from the galaxies and forms characteristic "cometary" tails. The radio continuum emission corresponds primarily to synchrotron radiation produced by relativistic electrons accelerated mainly in supernova explosions. Using data from the LoTSS project obtained with the LOFAR observatory, we study te presence of radio continuum emission and the morphology of these galaxies. We apply methods of image analysis and statistical processing, particularly local noise measurements and the construction of contour maps separating real emission from noise. Six jellyfish galaxies were not detected in the LOFAR data, while selected detected galaxies are analysed in detail with respect to their radio morphology. We also investigate how the width of the radio tails changes with distance from the galaxy center and compare the properties of the galaxies in radio continuum and Hα emission, which traces ionized gas. We find an approximately linear relation between the Hα flux and the total radio flux, qualitatively consistent with the known correlation between radio luminosity and star formation rate in spiral galaxies.

MUNI
SCI

MASARYKOVA UNIVERZITA
PŘÍRODOVĚDECKÁ FAKULTA
KOTLÁŘSKÁ 2, 611 37 BRNO
IČ: 00216224
DIČ: CZ00216224

ZADÁNÍ
BAKALÁŘSKÉ PRÁCE

Akademický rok: 2025/2026

Ústav:	Ústav teoretické fyziky a astrofyziky
Studentka:	Terézia Debnárová
Program:	Fyzika
Specializace:	Astrofyzika

Ředitel *ústavu* PřF MU Vám ve smyslu Studijního a zkušebního řádu MU určuje bakalářskou práci s názvem:

Název práce:	Struktury radiového kontinua u blízkých galaktických medúz
Název práce anglicky:	Radio continuum structures in nearby jellyfish galaxies
Jazyk práce:	angličtina

Oficiální zadání:
LOFAR (Low-Frequency Array) je evropský radiový interferometr pro pozorování na nízkých frekvencích 10-240 MHz. Jedním z jeho klíčových projektů je LoTSS (LOFAR Two-metre Sky Survey), který mapuje oblohu v pásmu kolem 144 MHz s vysokou citlivostí a rozlišením. V rámci LoTSS byly identifikovány desítky tzv. jellyfish galaxií v blízkých kupách, které vykazují ohony radiového kontinua - stopy po ram pressure strippingu, kdy je mezihvězdná hmota galaxie strhávána interakcí s horkým mezigalaktickým plynem. Radiové ohony vznikají jako synchrotronové záření vyzařované relativistickými elektrony, které pocházejí z tvorby hvězd v discích galaxií. Tyto struktury poskytují jedinečný pohled na dynamiku prostředí v kupách galaxií a na to, jak vnější podmínky ovlivňují vývoj galaxií. Cílem bakalářského projektu je seznámit se s fungováním observatoře LOFAR a analyzovat data získaná v rámci projektu LoTSS. V archivu projektu budou vyhledána zkalibrovaná data dostupná pro galaktické kupy Coma a Leo. V rámci jejich zpracování bude vytvořen celkový snímek kup zkombinováním překrývajících se polí a jejich přeškálováním podle úrovně šumu. S využitím nástrojů CARTA, DS9 či pomocí vlastních python skriptů bude identifikován a proměřen signál pro vzorek cca 20 jellyfish galaxií. Analýza bude zahrnovat měření základních vlastností ohonů radiového kontinua, jako je jejich jasnost, geometrie a morfologie. Tyto vlastnosti budou porovnány s optickým pozorováním v čáře $H\alpha$, která mapuje ionizovaný plyn, což pomůže popsat různé aspekty fyzikálních procesů probíhajících při ram pressure strippingu a interakci galaxií s okolním prostředím v kupách.

Vedoucí práce:	Mgr. Pavel Káchym, Ph.D.
Datum zadání práce:	21. 10. 2025
V Brně dne:	29. 4. 2026

Zadání bylo schváleno prostřednictvím IS MU.

Terézia Debnárová, 10. 11. 2025
Mgr. Pavel Jáchym, Ph.D., 24. 11. 2025
RNDr. Luboš Poláček, 11. 12. 2025

Poděkování

V prvom rade sa chcem poďakovať vedúcemu tejto práce Mgr. Pavlovi Jáchymovi, Ph.D. za ochotu, trpezlivosť, čas a neustálu pomoc počas písania tejto práce. Zároveň chcem poďakovať každému, kto mi akýmkoľvek spôsobom pomohol na tejto ceste. Ďakujem rodine, priateľovi a hlavne mojim rodičom, za nekonečnú podporu v štúdiu, pretože vďaka nim si môžem plniť tento sen. Poďakovanie patrí aj mojim kamarátom a spolužiakom, ktorí vytvorili to najkrajšie prostredie, ktoré mi nikdy nedovolilo vzdať sa. Špeciálne sa chcem poďakovať kamarátovi Samuelovi, ktorý ma do celého štúdia astrofyziky zasvätil a vždy mi podal pomocnú ruku.

Prohlášení

Prohlašuji, že jsem svoji bakalářskou práci vypracovala samostatně pod vedením vedoucího práce s využitím informačních zdrojů, které jsou v práci citovány.

Brno 13. května 2026 ....

Terézia Debnárová

Contents

List of Notations

EMR	Electromagnetic Radiation
EMS	Electromagnetic Spectrum
FWHM	Full Width at Half Maximum
ICM	Intra-cluster medium
ISM	Interstellar medium
RMS	Root Mean Square
RPS	Ram Pressure Stripping
WCS	World Coordinate System

Introduction

Galaxy clusters are the most massive gravitationally bound objects in the Universe, with masses of up to a thousand trillion times that of our sun and extending millions of light years across. They typically contain hundreds to thousands of member galaxies orbiting around the cluster's center point of gravity. These structures contain superheated plasma that permeates a galaxy cluster. It consists of a hot and dense ionised gas called the intra-cluster medium (ICM).

Galaxies within galaxy clusters rush through the ICM at orbital velocities typically of the order of 1000 km/s. Consequently, the intra-cluster medium applies external dynamical pressure on the gas inside the galaxies, which can result into efficient removal of the galaxy's interstellar matter (ISM). This process, known as ram pressure stripping, has a major influence on galaxy evolution in dense cluster environments, as it can deplete the gas reservoir required for future star formation. During this process, extended gaseous structures are formed behind the galactic disk, often resembling the tentacles of a jellyfish. These galactic tails consist of multiple gas phases and were observed also using radio interferometers, allowing us to see features that are not visible at other wavelengths.

At the beginning of this thesis, we focus on the fundamental background of radio astronomy and the process of ram pressure stripping. The subsequent section is dedicated to the specific properties of our selected jellyfish galaxies in relation to the radio continuum, providing a detailed description of the data processing and analysis. We conclude the thesis by comparison of the radio continuum results with Hα properties of the jellyfish sample.

Chapter 1

Radio astronomy

Radio astronomy is a subfield of astronomy that studies celestial objects at radio wavelengths. Since the 1930s, when the first radio signal from our galaxy was detected by Karl Jansky, astronomers have used radio waves to study the universe.

1.1 Electromagnetic spectrum

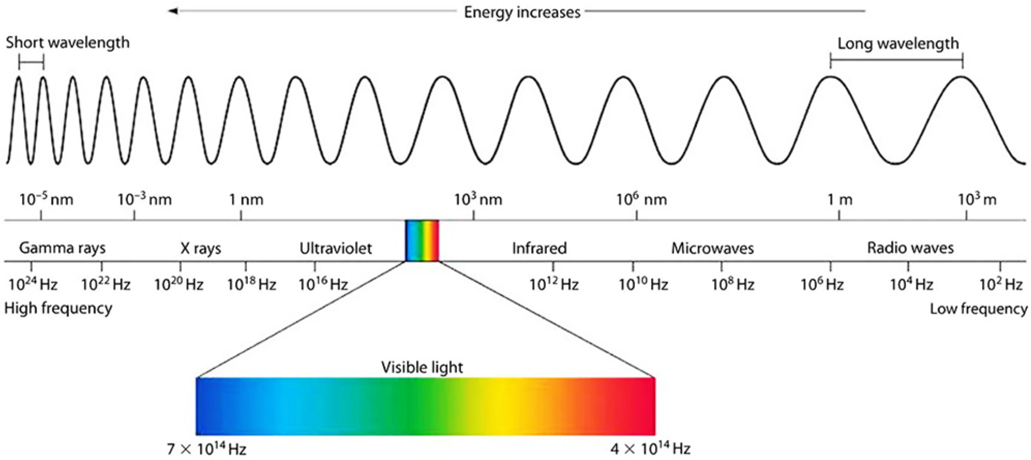

Figure 1.1: Electromagnetic spectrum

The electromagnetic spectrum encompasses all types of electromagnetic radiation (EMR). It can be expressed in terms of energy, wavelength, or frequency. The spectrum consists of many subranges, which bear different names and bands according to their behavior in emission, absorption, transmission, and practical use (see Figure 1.1) . Instead of borders between these portions, they fluently flow into each other. All the types of EMR are spread at the same speed in a vacuum — the speed of light marked as c. This phenomenon is described by the equation

$$c = \lambda \cdot f, \tag{1.1}$$

where λ is the wavelength and f is the frequency of EMR.

EMR can also be conceptualized as a stream of discrete energy packets called photons. Photons possess both wave and particle characteristics. Their particle-like behavior is most prominent at high frequencies, such as X-rays or Gamma rays. In contrast, the wave-like character is observed at much lower frequencies, for instance, in the radio or microwave bands. High-frequency waves have high-energy photons, while low-frequency waves have low-energy photons.

1.1.1 Radio band

The radio spectrum is a crucial part of modern communication technologies, as well as space science and astronomy. It refers to the portion of the electromagnetic spectrum spanning roughly from a few hertz to hundreds of gigahertz. These frequencies are divided into classes from very low frequencies to extremely high frequencies, and we can find them at the longest wavelengths in EMS. Radio astronomers have a major advantage as they are able to conduct observations directly through interstellar dust, unlike optical observations that do not allow us to see through as they get absorbed and scattered by the dust particles. But even for this method, obstacles appear. The atmosphere absorbs the incoming signal and converts it into heat. At low frequencies, transmission is limited by the ionosphere, while at higher frequencies, water vapor interferes with radio astronomy. This is the reason why low-humidity sites, with extremely dry air and high altitude, are used for observations. We define a “window” whose range is from 15 MHz to 1 THz, and in this band, the atmosphere is partially transparent and ground-based observations are possible.

1.2 LOFAR - Low Frequency Array

LOFAR (Low-Frequency Array) is an European radio telescope, operating at low frequencies ranging from 10 - 240 MHz (Haarlem et al. 2013). It provides a number of unique observing capabilities allowing to achieve unprecedented levels of resolution and sensitivity at low frequencies. The several technical challenges (hardware, data transport, data calibration) faced by LOFAR make this instrument an important pathfinder for the Square Kilometer Array (SKA), which is going to be the largest and most powerful astronomical observatory in the near future. It is a system of thousands of simple dipole antennas deployed across Europe, where the central core is situated in the Netherlands. The network involves many stations, providing baselines up to more than 1000 km. There are two types of antennas at each station: the High Band Antennas (HBA, 110 – 240 MHz) and Low Band Antennas (LBA, 10 – 90 MHz). Instead of using moving dishes, LOFAR performs observations electronically: signals from all antennas are digitized and combined through interferometric correlation and beamforming techniques, allowing the array to simulate a single radio telescope with very high angular resolution.

1.2.1 Science with LOFAR

The multi-beaming capabilities of the LOFAR telescope allow astronomers to conduct research across a broad range of fields. Besides galaxy evolution in cluster environment

Figure 1.2: The Dutch core of the LOFAR interferometer (Vajiram Content Team)

(the goal of this project), scientists are able to study various cosmic phenomena. One of the projects is focused on the Epoch of Reionization (EoR), the period during which the neutral gas in the universe was completely ionized by the first stars and galaxies.

Its exceptional sensitivity enables LOFAR to make detailed studies of pulsars and transient sources. Recently, astronomers discovered LOFAR's first "blind" transient in the direction of the north celestial pole, measured the low-frequency spectrum of radio emission from a nearby black hole (V404 Cyg) in outburst, and followed up on the first detection of gravitational waves. Apart from that, solar science, space weather, and cosmic magnetism are also key areas for LOFAR targeting.

1.2.2 Project LoTSS

The LOFAR Two-metre Sky Survey (LoTSS) is one of the main results of the LOFAR Survey Key projects. It is a wide-area continuum survey that covers the entire northern sky in the range of 120 – 168 MHz using high-band antennas at the full resolution of the Dutch core stations LOFAR (6 arcseconds) and a declination-dependent sensitivity which will typically be around 100 μJy/beam (Shimwell, Röttgering, et al. 2017; Shimwell, Tasse, et al. 2019; Shimwell, Hardcastle, Tasse, Best, et al. 2022). This project includes different types of polarizations :

- **Stokes I (total intensity):** The maps have a highest angular resolution of 6" and sensitivity of 83 μJy/beam. They are primarily used for the detection and cataloging of radio sources.

- **Stokes V (circular polarization):** The maps have a lower angular resolution of 20" and sensitivity of 95 μJy/beam. The purpose is to study circular polarization, which is typically weaker and more challenging to detect than total intensity.

- **Stokes Q and Stokes U (linear polarization):** The sensitivity is 10.8 mJy/beam with an angular resolution of 4’ and 2.2 mJy/beam with an angular resolution of 20”.

This bachelor’s thesis works with the Stokes I maps from the LoTSS survey Data Release 2, in which data covering 27% of the northern sky and reaching a median rms sensitivity of 83 μJy/beam were published. Currently, Data Release 3 covering 88% of the northern sky has been released (Shimwell, Hardcastle, Tasse, Drabent, et al. 2026).

Chapter 2

Jellyfish galaxies

Jellyfish galaxies are named for the long, tentacle-like streams of gas and young stars that trail behind them. They are formed in galaxy clusters when they move quickly through a hot and dense intracluster environment. This interaction acts like a strong wind pushing the jellyfish galaxy´s own interstellar gas out of the disk, forming extended trails. The technical term for the process that creates these galaxies is called ram-pressure stripping.

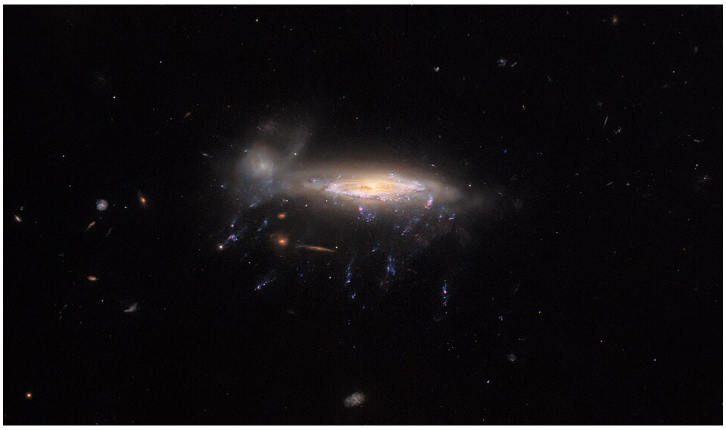

Figure 2.1: Jellyfish galaxy PGC29820 in cluster Abell 957, captured by the Hubble Space Telescope, showing long tendrils of gas and star-forming regions stripped away by ram pressure. credit: ESA/Hubble & NASA

2.1 Ram-pressure stripping

Ram pressure (RPS; Gunn and Gott 1972) stripping is one of the most efficient environmental mechanisms driving the evolution of galaxies in dense cluster environments. This hydrodynamical process arises from the relative motion between satelite galaxies and the intracluster medium (ICM). As a galaxy moves through the ICM, its interstellar medium (ISM) experiences external pressure that can heat, evaporate (Cowie and Songaila 1977), or directly remove gas from the galactic disk through ram pressure (Gunn and Gott 1972). In addition, turbulent instabilities developing at the contact point between the cold gravitationally bound ISM and hot surrounding ICM further enhance and accelerate the stripping process.

Galaxies falling into clusters are expected to experience a pressure of

$$P = \rho_{\mathrm{ICM}} v^2 \tag{2.1}$$

where ρ_{ICM} is the intracluster gas density and v is the speed of the galaxy relative to the medium (Boselli, Fossati, and Sun 2022). If the ram pressure is sufficiently strong to exceed the galaxy's gravitational potential, the galaxy loses its gas, which is effectively stripped from the disk.

Objects undergoing RPS are characterized by one-sided tail of stripped material. Depending on the gas phase (atomic, molecular, or ionized), these tails are observable at multiple wavelengths. The atomic component often reveals the most extended structures, showing how loosely bound gas is first removed from the galaxy's outskirts. In contrast, the molecular phase represents the dense, cold reservoirs that can either be stripped directly or form in-situ within the tail through the cooling of more diffuse gas. Finally, the ionized phase, frequently observed via Hα emission, highlights regions of intense heating or active star formation, tracing the ”tentacles” where young stars are born from the stripped material. This astrophysical phenomenon has an impact on galaxy evolution (Lee et al. 2022).

2.1.1 Radio continuum component

Jellyfish galaxies can exhibit spectacular multiphase tails, together with tails of relativistic particles and magnetic fields visible through radio continuum emission (Roberts, Weeren, Lal, et al. 2023).

The radio continuum component is primarily produced by synchrotron radiation emitted by relativistic electrons spiraling around magnetic field lines. These cosmic ray electrons are mainly accelerated in supernova remnants associated with recent star formation in the galactic disk, although additional acceleration may occur in shocks and turbulent regions generated by the stripping process itself.

During ram pressure stripping, not only gas but also cosmic rays and magnetic fields can be displaced from the galaxy, forming extended radio continuum tails that often coincide with the stripped gaseous material.

2.2 Coma cluster

Galaxy clusters are the largest gravitationally bound structures in the universe. One prominent example is the Coma cluster, also known as Abell 1656, located at a distance of 100 Mpc from us. Coma cluster is a massive galactic cluster with a viral mass of $1.4 \cdot 10^{15}\,\mathrm{M}_{\odot}$ and virial radius of 2.8 Mpc (Malavasi et al. 2020). This cluster lies near the North Galactic Pole within the constellation of Coma Berenices and contains more than a thousand identified galaxies. The cluster is dominated by elliptical and lenticular galaxies, especially in its dense central region, where the galaxy population mainly consists of old stars with little ongoing star formation. Farther out from the center of the cluster, spiral galaxies are more common and often contain significant reservoirs of cold gas and dust, providing favorable conditions for new star formation.

Figure 2.2: Coma cluster of galaxies in X-ray and optical light, revealing the distribution of the intracluster medium and the galactic population, respectively; credit: ESA/XMM-Newton/SDSS/J. Sanders et al. 2019

In our research, we study a sample of 18 jellyfish galaxies which are listed along with other parameters in Table 2.1. The sample galaxies were selected from the ALMA JELLY project (PI: P. Jáchym), which investigated the molecular gas content of jellyfish galaxies in the nearby Coma, Leo, and Norma clusters. Their galaxy sample was selected based on the presence of prominent Hα tails produced by ram-pressure stripping, indicating ongoing interactions between the galaxies and the intracluster medium. The stellar masses of the sample galaxies were adopted from the review paper by (Boselli, Fossati, and Sun 2022).

According to the SIMBAD database, the center of the Coma galaxy cluster has the following ICRS coordinates

RA = 12:59:44.40

DEC = +27:54:44.9

For each galaxy, we determined physical distances in kpc from the cluster centre by subtracting the right ascension α and declination δ coordinates. It was necessary to convert coordinates from hours/minutes/seconds format into decimal degrees. The spherical distance is calculated using the small-angle approximation formula

$$\theta = \sqrt{(\Delta\alpha \cdot cos\delta)^2 + (\Delta\delta)^2}, \tag{2.2}$$

where $\Delta\alpha$ is the difference in RA, $\Delta\delta$ is the difference in DEC, and δ represents the declination of the cluster center.

Assuming a uniform distance of R = 100 Mpc for all galaxies as well as for the cluster centre itself, the physical distance is defined by

$$R_{\text{cen}} = R \cdot \theta \tag{2.3}$$

Redshift values for all galaxies were retrieved from the SIMBAD astronomical database and subsequently used to calculate the optical velocity according to the following formula

$$v_{\text{opt,gal}} = c \cdot z, \tag{2.4}$$

where z is a redshift and c is the speed of the light.

The optical velocity of the galaxy cluster center was obtained from the SIMBAD database:

$$v_{\text{opt,cen}} = 7015\ \text{kms}^{-1}$$

This value was subsequently subtracted from the optical velocities of the individual galaxies cz_{gal} to calculate the radial velocity of the galaxies v_{r} within the cluster according to the following relationship:

$$v_{\text{r}} = v_{\text{opt,gal}} - v_{\text{opt,cen}} \tag{2.5}$$

A complete overview of the calculated values for the entire sample of galaxies is provided in Table 2.1.

Table 2.1: Parameters of the jellyfish galaxies in the Coma cluster

Name	RA	DEC	$\log M_*$ $[M_\odot]$	R_{cen} [kpc]	$v_{\text{opt,gal}}$ $[\text{km}\,\text{s}^{-1}]$	v_{r} $[\text{km}\,\text{s}^{-1}]$
GMP 2910	13:00:09.14	27:51:59.34	9.26	180.8	5315.3	-1699.7
NGC 4848	12:58:05.58	28:14:33.26	10.32	860.6	7024.5	9.5
GMP 4060	12:58:42.59	27:45:37.79	9.12	473.4	8747.9	1732.9
IC 4040	13:00:37.87	28:03:28.68	9.65	422.6	7653.7	638.7
IC 3949	12:58:55.77	27:49:58.93	10.42	341.8	7524.8	509.8
GMP 3779	12:59:05.29	27:38:39.85	9.74	531.0	5435.2	-1561.8
GMP 3071	12:59:56.17	27:44:47.30	8.90	301.3	8921.8	1906.8
GMP 4232	12:58:30.62	27:33:51.50	7.39	771.9	7283.0	268.0
NGC 4911	13:00:56.06	27:47:27.15	10.89	509.3	7971.5	956.5
GMP 2923	13:00:08.06	27:46:23.94	8.75	284.1	8670.0	1655.0
GMP 3016	13:00:01.03	28:04:54.78	7.49	314.9	7765.0	750.0
GMP 3271	12:59:39.81	27:34:35.78	9.20	587.7	5009.5	-2005.5
NGC 4858	12:59:02.12	28:06:55.94	9.40	446.3	9416.5	2401.5
NGC 4853	12:58:35.20	27:35:46.97	10.37	708.5	7686.7	671.7
GMP 4629	12:57:50.24	28:10:13.29	8.47	860.8	6919.2	-95.8
GMP 4570	12:57:56.80	27:59:30.31	8.53	701.3	4565.8	-2449.2
GMP 4555	12:57:57.75	28:03:41.50	9.75	730.0	8136.4	1121.4
NGC 4854	12:58:47.43	27:40:28.89	10.67	522.2	8382.2	1367.2

Chapter 3

Data analysis

3.1 Software and scripts

Several software tools and applications were used for the data processing and analysis presented in this work. We used SAOImageDS9 8.6 (SAOImageDS9 download) for image visualization and employed its various built-in tools to measure galaxy parameters.

To calculate local noise levels for all galaxies in the LoTSS image, we developed a custom Python script. Contour maps were then generated based on these noise calculations and subsequently plotted using additional Python-based script. The individual techniques are described in more detail in the following sections.

Data regarding object properties were obtained from the SIMBAD database (SIMBAD Astronomical Database) and SDSS website (Sloan Digital Sky Survey).
Additional information was gathered from relevant scientific publications.

Images of individual galaxies were prepared by cropping the original LoTSS wide-field images in Python to focus on the target galaxies and their surroundings.

3.2 Datasets

The data processed in this thesis are available in the public archive LoTSS Data Release 2 (DR2). The DR2 data were processed through calibration pipelines that correct for instrumental effects as well as spatially and temporally varying ionospheric distortions. We worked with a mosaic covering the full extent of the Coma Cluster, produced by combining three observing pointings using noise-weighted imaging techniques. The final mosaic was kindly provided by I. D. Roberts. (see Figure 3.1), which served as the primary dataset for our entire analysis. Additionally, a smoothed, 12 arcsec resolution version of this mosaic was generated by convolving the image to a lower angular resolution for comparative purposes. Analyzing smoothed LOFAR images provides improved sensitivity to faint, diffuse radio continuum emission that may be difficult to detect in the original high-resolution 6 arcsec maps. The thesis also includes optical images, which were retrieved from the Legacy survey archive using Python scripts.

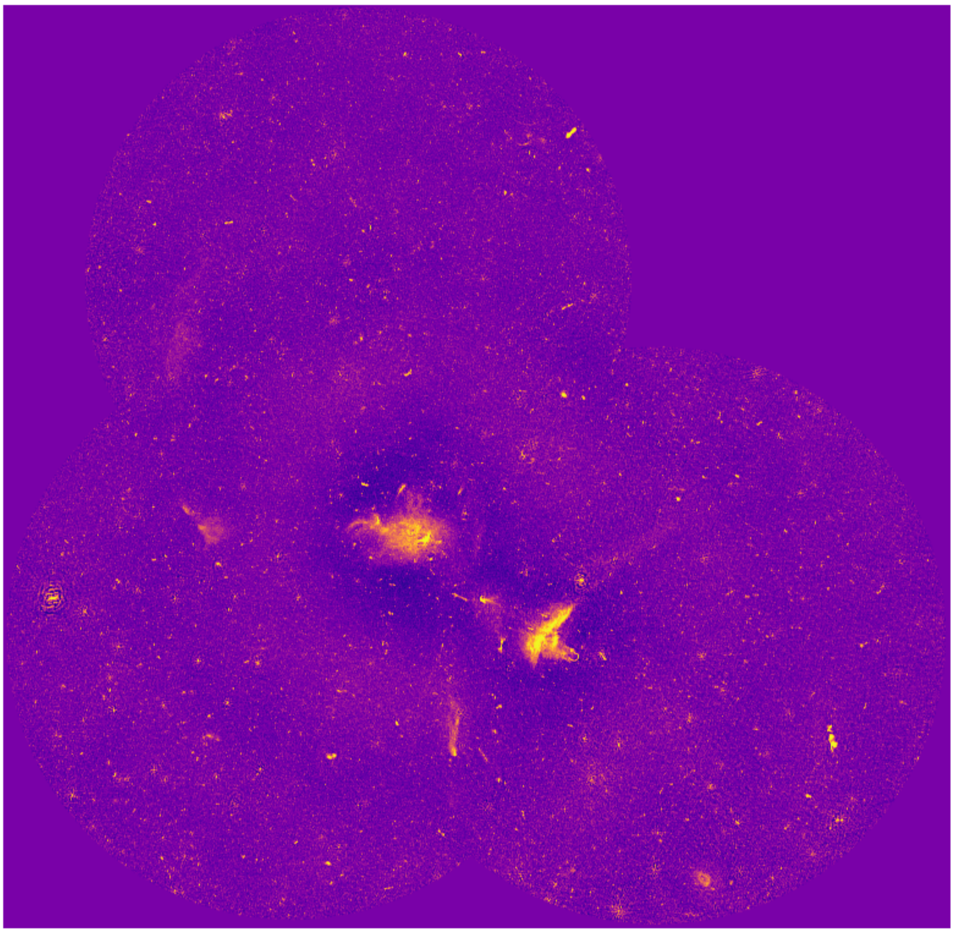

Figure 3.1: LOFAR 144 MHz image mosaic of the Coma cluster (courtesy of I.D.Roberts).

3.3 Regions of jellyfish galaxies

To enable a detailed study of the aforementioned jellyfish galaxies, it was necessary to extract them individually from the original large-scale mosaic Figure 3.1. The mosaic image was loaded into Python along with the galaxy coordinates (see Table 2.1). A crucial step in this process was the application of the World Coordinate System (WCS), a mathematical framework that maps image pixels to celestial coordinates. Each galaxy was cropped into a 600 × 600 pixel which is 15 arcmin × 15 arcmin image. Finally, a scale bar was plotted on each image to represent the angular scale in arcminutes. All processed galaxy images are included in the Appendix Figure 4.5.

3.4 Noise estimates

The noise level (i.e., the sensitivity) is not uniform across the mosaic. This is caused by the combining of multiple pointings, primary beam corrections, calibration uncertainties, but also the presence of nearby bright radio sources that increase imaging artefacts and sidelobe noise (see Figure 3.1). Since we aim to consistently provide and measure the radio emission of our galaxies, measuring the local noise RMS (Root Mean Square) in the LOFAR map at the positions of individual galaxies is necessary. This will enable reliable estimates of the detection significance and contours to be defined consistently for each galaxy. The crucial step is to define a basic signal level, which we will use for measuring, which is interpreted as a multiple of the RMS noise. We explored several ways to measure the noise locally in the locations of our galaxies. We choose a region of $5' \times 5'$ around each galaxy. Galaxies are always situated at the centre of the image. Values from all calculated methods are in the Table 3.1. All these steps were calculated in Python.

3.4.1 Methods

Standard deviation

Standard deviation is a measure of how much the pixel brightness values vary within the selected image region. It is highly sensitive to outliers and non-Gaussian features in the data. In this case, the value of the standard deviation is artificially increased because of the bright galaxy itself, but also the presence of background structures. We provided just a standard deviation calculation of the pixel intensity distribution:

$$\sigma = \sqrt{\langle (I - \bar{I})^2 \rangle}, \tag{3.1}$$

where I represents the individual pixel intensities and $\bar{I}$ is the mean intensity within the selected field.

Sigma clipping

To obtain a robust estimate of the background noise, we employed an iterative sigma-clipping algorithm. This process is a statistical method used to remove noise or outliers from the data. The primary condition for a pixel to be retained in the dataset during each iteration is defined by the inequality

$$|I_i - \mu_n| \leq N \cdot \sigma_n, \tag{3.2}$$

where I_i is the intensity of an individual pixel, μ_n is the mean intensity of the pixels in the n-th iteration, N is the clipping threshold and σ_n is the standard deviation of the pixels in the n-th iteration.

The final estimate of the background noise is then defined as the standard deviation obtained after the last iteration:

$$\sigma_{\text{clipp}} = \sigma_k, \tag{3.3}$$

where k is the total number of performed iterations.

We perform this calculation in several steps.

- Calculating Basic Statistics: The mean μ and standard deviation σ are calculated for the dataset.
- Setting the Threshold: We defined a sigma multiplier as 3σ. That means that any data point falling outside the settled range of $\pm\, 3\sigma$ is considered noise.
- Rejection (Clipping): We excluded data points outside this range from the dataset.
- Iteration: The mean and sigma are recalculated from the new dataset. We pre-set 10 iterations. So this process repeats until the pre-set number of iterations is reached.

Median Absolute Deviation (MAD)

Median absolute deviation (MAD) is a robust estimator of the background noise and is far less sensitive to extreme values, compared to standard deviation. It is formulated as

$$\mathrm{MAD} = \mathrm{median}(|I_i - \tilde{I}|), \tag{3.4}$$

where I_i is the value of i-th pixel in the region and $\tilde{I}$ is a median of all the pixels in the region. The MAD value itself is not directly comparable to the noise σ. To relate the MAD to the standard deviation of a Gaussian distribution, we applied a consistency factor with a value of 1.4826. The final equation for this method is

$$\sigma_{\mathrm{MAD}} = 1.4826 \times \mathrm{MAD} \tag{3.5}$$

The calculation was performed in these four steps.

- Find the Median: We calculated the median of all data points.
- Calculate Deviations: Find the difference between each pixel value and the median.
- Find the Median of Deviations: The MAD is the median of the absolute values of these differences.
- Scale to standard deviation: The result was multiplied by a constant factor.

After evaluating these three noise estimation methods, we selected the one that provided the most consistent results. The values obtained via standard deviation significantly deviated from the other two methods (see Table 3.1) due to their sensitivity to outliers. When comparing the σ_{clipp} and σ_{MAD} results, we opted for the sigma-clipping method, as it provides a more refined convergence to the true background noise. The resulting estimates exhibit a more stable and nuanced distribution, capturing the background characteristics more accurately. The result of this method is a cleaned RMS value, which we consider to be representative of the level of background noise in our data.

$$\mathrm{RMS} = \sigma_{\mathrm{clipp}} \tag{3.6}$$

Consequently, we adopted this method for all subsequent analyses and calculations in our work.

Table 3.1: Calculated values of local noise

Name	σ	σ_{clipp}	σ_{MAD}
$\cdot 10^{-5}$ [Jy/beam]			
GMP 2910	11.07	9.26	9.62
NGC 4848	71.36	9.04	9.24
GMP 4060	18.26	8.21	8.30
IC 4040	76.48	13.56	13.83
IC 3949	17.41	10.30	10.48
GMP 3779	19.23	7.82	8.00
GMP 3071	24.76	8.89	8.97
GMP 4232	22.79	8.07	8.26
NGC 4911	43.64	8.31	8.67
GMP 2923	11.81	8.56	8.74
GMP 3016	10.41	9.27	9.46
GMP 3271	8.98	7.59	7.68
NGC 4858	34.85	8.99	9.26
NGC 4853	15.91	7.96	8.14
GMP 4629	8.56	7.94	7.94
GMP 4570	8.63	7.97	8.07
GMP 4555	181.51	9.25	9.44
NGC 4854	32.02	8.09	8.32

3.5 Contour maps

The next crucial step in our analysis was to visualize the galaxies in a way that would allow for more precise measurements. Utilizing the previously calculated background noise levels obtained via sigma-clipping (see Section 3.4.1), we were able to define the boundaries of the galaxies using specific contour levels. We defined a field of view of $5' \times 5'$ for our cropped LOFAR images and established isophotal contours based on the specific local RMS noise level calculated for each galaxy. The levels of countours are defined as

$$C_i = n_i \cdot \text{RMS}, \tag{3.7}$$

where n_i is the value of the i-th contour, and RMS is the calculated background noise value.

We selected two different base levels to show the faintest parts of the galaxy. The first version starts at a threshold of 2×RMS, while the second starts at 4×RMS.

For better analysis and visualization, we zoomed in on our galaxies in Figure 4.5 and displayed six logarithmic contour levels for each galaxy, starting at

2×RMS (2, 4, 8, 16, 32, 64)

4×RMS (4, 8, 16, 32, 64, 128)

For this procedure, including field zooming, calculating and outlining contours, we used a python-based script implementing equation 3.7, together with contouring routine for image visualization. As a result, these images can be seen in Figure 3.3 and Figure 3.4.

Following the same methodology, we generated contours for the smoothed data for comparison. The results can be found in Figure 4.6 and Figure 4.7 in Appendix.

3.5.1 Overlays on optical images

Using the CDS HiPS2fits service in Python, we retrieved optical images of all 18 galaxies from the Legacy Survey (Dey et al. 2019) and overlaid them with radio contours to compare the optical and radio regions. All images can be found in the Appendix Figure 4.8 for the 2×RMS version and Figure 4.9 for the 4×RMS version. Figure 3.2 shows an example overlay image for the galaxy NGC 4848.

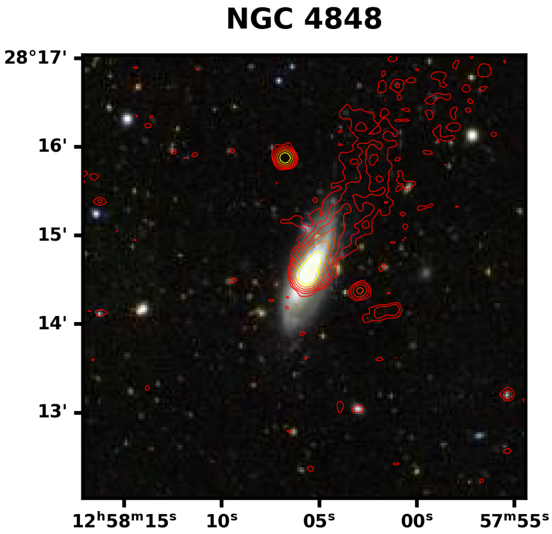

Figure 3.2: Overlaid galaxy NGC 4848 with 2×RMS radio contours

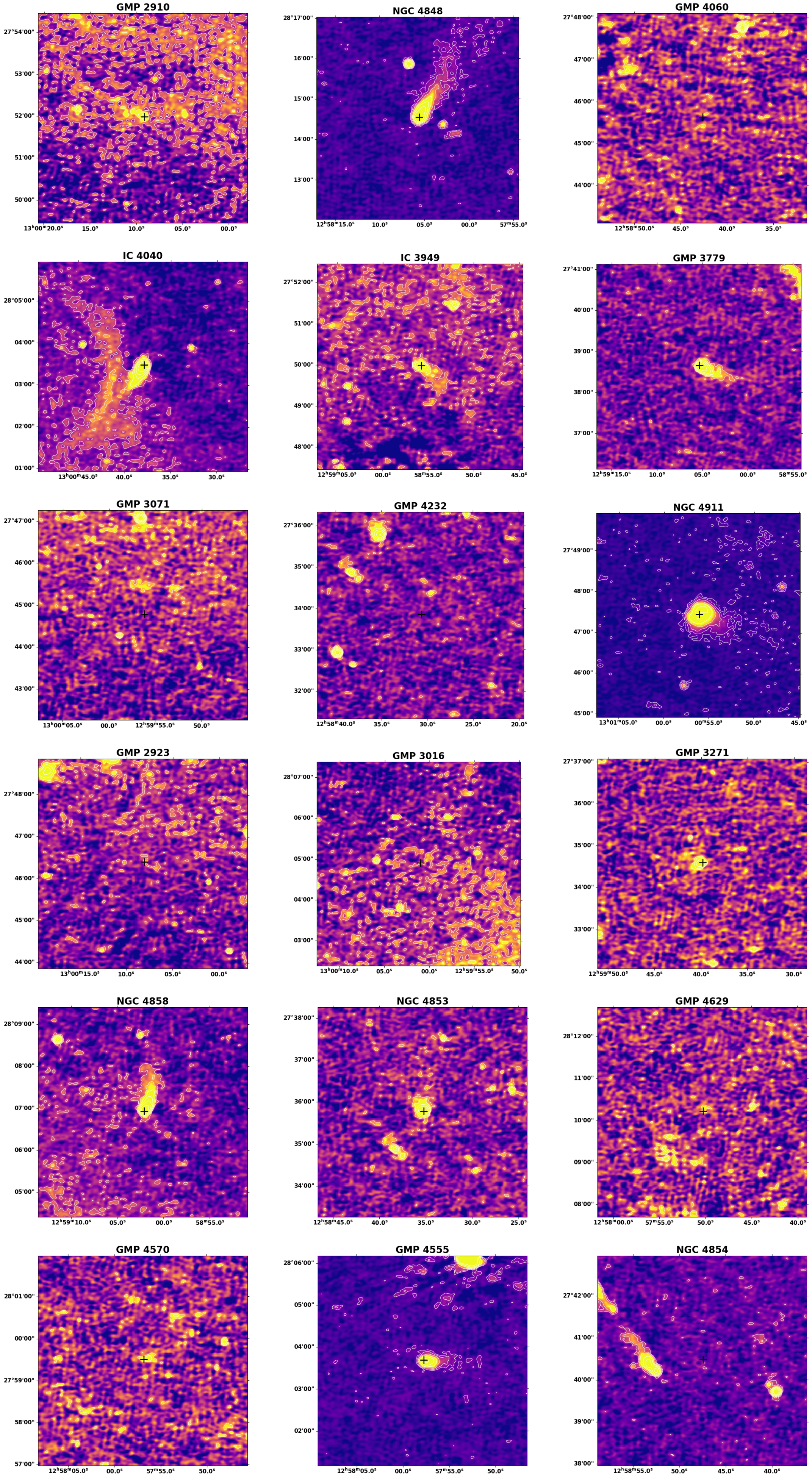

Figure 3.3: Overview of galaxies with rendered contours for the 2× RMS version

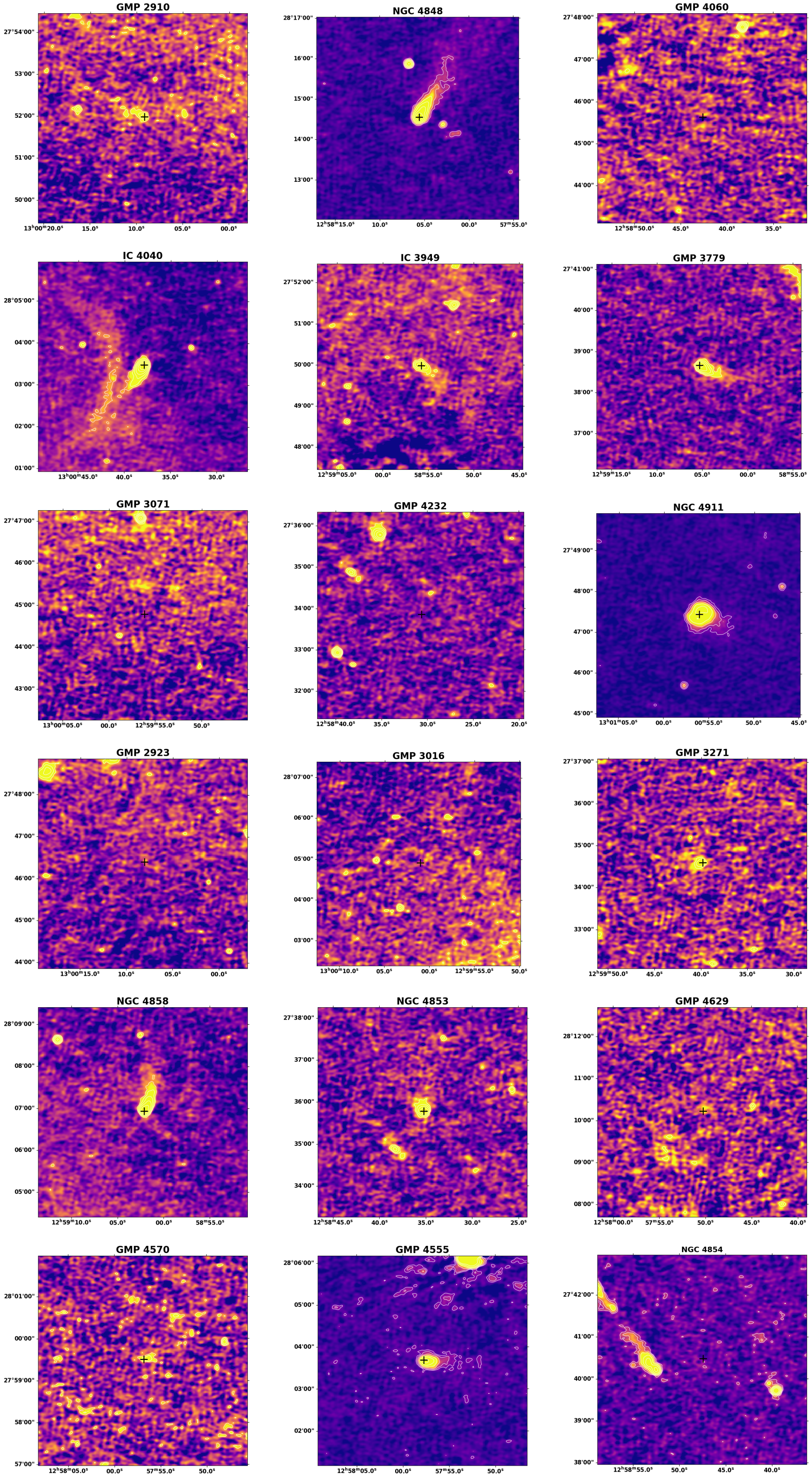

Figure 3.4: Overview of galaxies with rendered contours for the 4× RMS version

3.6 Radio continuum properties of galaxies

Inspection of the radio continuum contour maps shown in Figure 3.3 and Figure 3.4 reveals that radio emission is detected in 12 galaxies from our sample (see Table 3.2). In this subsection, we present the measurements of the radio continuum properties of our sample galaxies, specifically their morphology, geometry, and total radio continuum emission. After determining the RMS values (see Table 3.1) using the sigma-clipping method (see Section 3.4.1) and establishing the lowest contour levels, we visually identified which galaxies were suitable for more detailed parameter measurements. We selected galaxies with prominent tails—specifically, six galaxies in the $2 \times$ RMS version and seven in the $4 \times$ RMS version. For the galaxies exhibiting clearly extended radio continuum tails, we determine basic tail properties, including their projected lengths and widths. As shown in the contour maps Figure 3.3 and Figure 3.4, six galaxies were not detected by LOFAR. From the LOFAR 144 MHz images, we first measure in Section 3.6.1 the total integrated flux densities of individual galaxies in units of Jy and estimate upper limits for non-detected sources.

3.6.1 Integrated flux densitites

For the galaxies that were easily identified as detected in the contour maps, we obtained the total flux density values (see Table 3.2). Using the SAOImage DS9 software, where we plotted contours with the lowest levels corresponding to $2\times$RMS and $4\times$RMS, and applying the *Polygon* tool, we traced the entire region of the galaxy as accurately as possible. From the region statistics, we were able to obtain the total flux density within the region. The illustration of the process is shown in Figure 3.5 and Figure 3.6.

Since the LOFAR map is in Jy/beam units, the raw pixel sum which we obtained is not yet a true integrated flux density in Jy. The sum of pixel values in the region needs to be multiplied by a factor corresponding to the ratio of pixel area to beam area. As we show in 3.8, the beam area is about 40.8 arcsec^2, while the pixel area is simply $(1.5 \text{ arcsec})^2 = 2.25$ arcsec^2. The factor is then 0.055.

For the cases where no clear source was detected in the radio continuum at the location corresponding to the optical center of the galaxy, we determined an **upper limit**.

This method establishes that if the galaxy is indeed emitting radiation, its flux must be lower than this specific value; otherwise, it would have been visible in our observations. The values calculated for the upper limit are listed in and Table 3.2. The estimates of the upper limit were calculated using the following equations:

Effective beam area

The radio beam is not a simple disk but follows a Gaussian profile. Its integrated area (A_{beam}) is calculated as

$$A_{\text{beam}} = \frac{\pi \cdot \theta_{\text{beam}}^2}{4 ln 2}, \tag{3.8}$$

where θ_{beam} is the full width at half maximum of the radio telescope beam with value of 6 arcsec and the factor $4 \ln 2 \approx 2.77$ accounts for the integration of the 2D Gaussian shape.

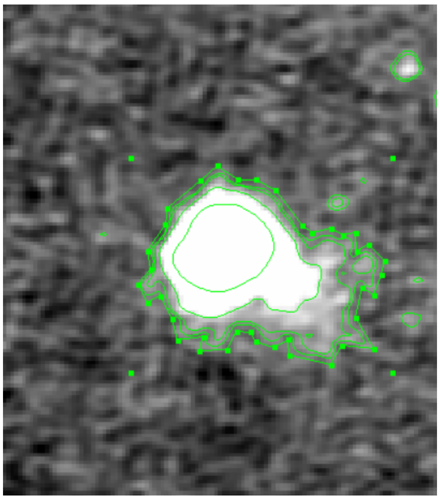

Figure 3.5: The process of measuring the integrated flux density of the 2×RMS version of the galaxy NGC 4911

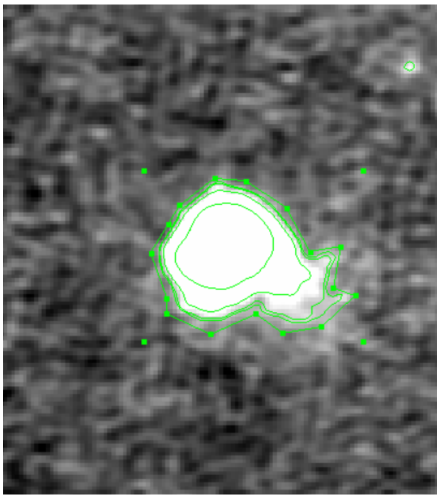

Figure 3.6: The process of measuring the integrated flux density of the 4×RMS version of the galaxy NGC 4911

Galaxy surface area

Assuming simply the galaxy has a roughly circular projection on the sky, its area is defined by

$$A_{\mathrm{gal}} = \pi \cdot r_{\mathrm{Petro,r}}^2, \tag{3.9}$$

where $r_{\mathrm{Petro,r}}$ is the Petrosian radius of the galaxy. These values were obtained from the SDSS database.

The scaling area factor

Since the galaxy is often larger than the beam (an extended source), the noise contributes across the entire area of the object. When summing independent noise elements, the total uncertainty increases with the square root of the number of beams covering the source

$$f_{\mathrm{area}} = \sqrt{\frac{A_{\mathrm{gal}}}{A_{\mathrm{beam}}}} \tag{3.10}$$

Final upper limit calculation

The resulting value represents the maximum possible flux the galaxy could have while remaining ”invisible” to our current observations defined by formula

$$S_{\mathrm{ul}} = n \cdot \mathrm{RMS} \cdot f_{\mathrm{area}}, \tag{3.11}$$

where n is a threshold (in our case 2 and 4).

Table 3.2: Measured flux values and estimated upper limits of our galaxies

name	$r_{\mathrm{Petro,r}}$ [$''$]	flux 2×RMS [Jy]	flux 4×RMS [Jy]	LOFAR detected
GMP 2910	6.41	$< 3.296 \cdot 10^{-4}$	0.00671	✓
NGC 4848	18.16	0.091410	0.12172	✓
GMP 4060	10.87	$< 4.954 \cdot 10^{-4}$	$< 9.908 \cdot 10^{-4}$	×
IC 4040	10.06	$< 7.572 \cdot 10^{-4}$	0.1010	✓
IC 3949	16.31	0.0196	0.0126	✓
GMP 3779	15.99	0.0249	0.0231	✓
GMP 3071	6.92	$< 3.413 \cdot 10^{-4}$	$< 6.826 \cdot 10^{-4}$	×
GMP 4232	8.80	$< 3.944 \cdot 10^{-4}$	$< 7.887 \cdot 10^{-4}$	×
NGC 4911	25.19	0.1271	0.1202	✓
GMP 2923	6.80	$< 3.230 \cdot 10^{-4}$	$< 6.461 \cdot 10^{-4}$	×
GMP 3016	9.11	$< 4.686 \cdot 10^{-4}$	$< 9.371 \cdot 10^{-4}$	×
GMP 3271	9.18	0.0041	0.0036	✓
NGC 4858	8.14	0.0535	0.0472	✓
NGC 4853	7.89	0.0162	0.0146	✓
GMP 4629	8.36	0.0004	$< 7.372 \cdot 10^{-4}$	✓
GMP 4570	7.33	0.0017	0.0007	✓
GMP 4555	12.20	0.0392	0.0037	✓
NGC 4854	23.21	$< 1.042 \cdot 10^{-4}$	$< 2\ .083 \cdot 10^{-4}$	×

3.6.2 Projected tail length

In this section, we investigate the tail lengths of our target galaxies. We specifically selected galaxies that exhibit clearly visible tail structures. In the $2 \times$ RMS version, we detected 6 galaxies with extended tail emission, while in the $4 \times$ RMS version, the number increased to 7. The procedure for determining this parameter was similar to the one described in the previous section. We used the SAOImage DS9 software to visualize the cropped images (see Figure 4.5), overlay contours corresponding to the calculated lowest levels σ_{clipp} (see Table 3.1), and applying the *Cross* region, identify the galaxy center at the corresponding coordinates. Finally, the *Ruler tool* was used to measure the distance from the center to the edge of the first contour in the direction of the tail (see Figure 3.7 and Figure 3.8).

In DS9, angular distances in degrees were measured. For better visualization and subsequent comparison, we converted these values into kpc. All values are in the Table 3.3 and Table 3.4.

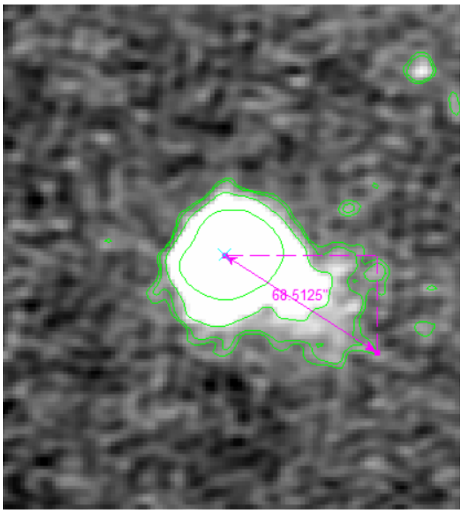

Figure 3.7: The process of measuring the tail length of the 2×RMS version of the galaxy NGC 4911

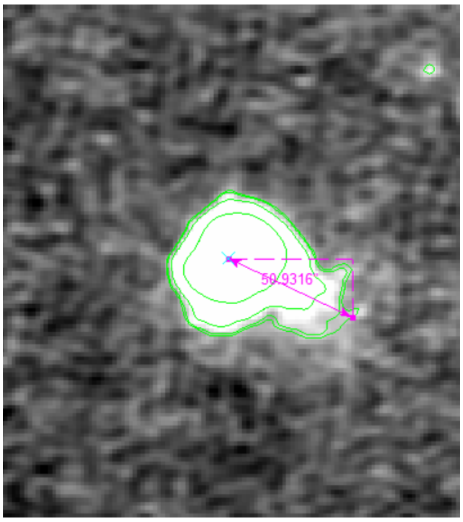

Figure 3.8: The process of measuring the tail length of the 4×RMS version of the galaxy NGC 4911

Table 3.3: Values of tail length of the galaxies with 2×RMS version

Name	l_{tail} [arcsec]	l_{tail} [kpc]
NGC 4848	188.92	90.68
IC 3949	50.55	24.26
GMP 3779	19.91	9.56
NGC 4911	68.51	32.89
NGC 4858	66.10	31.73
GMP 4555	47.35	22.73

Table 3.4: Values of tail length of the galaxies with 4×RMS version

Name	l_{tail} [arcsec]	l_{tail} [kpc]
NGC 4848	96.67	46.40
IC 4040	44.05	21.14
IC 3949	17.07	8.19
GMP 3779	34.56	16.59
NGC 4911	50.93	24.45
NGC 4858	43.19	20.73
GMP 4555	36.139	17.35

3.6.3 Projected width

Another parameter we studied is the galaxy width. For this measurement, we employed two different methods and subsequently compared their results. The analysis was primarily conducted using SAOImage DS9 software and Python.

Our cropped images (see Figure 4.5) were loaded into DS9, where we displayed the contours and identified the galaxy center following the same procedure used for the tail length measurement (see Section 3.6.2).

The first method involved defining a series of rectangular regions along the entire length of the galaxy using the *Projection* tool. The regions were oriented perpendicular to the tail direction. The width of these boxes was set to 6 arcsec for each galaxy, corresponding to the beam size. For consistency, the length of the regions remained constant for a given galaxy. The proccess of this measurement is shown in Figure 3.9 and Figure 3.10.

The following key step was to extract and save the intensity profile measured along each individual region. Subsequently, these profile data were loaded into Python to calculate the Full Width at Half Maximum (FWHM) by fitting a Gaussian function

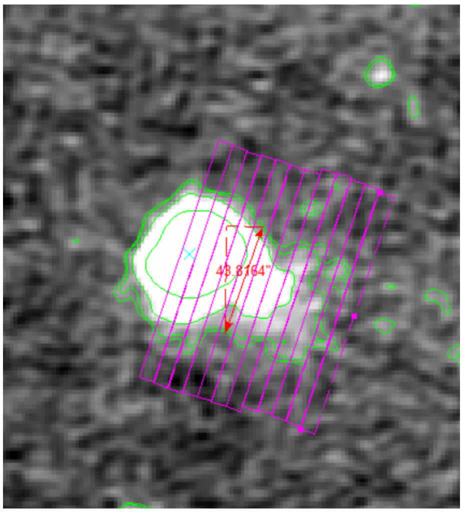

Figure 3.9: The process of measuring the tail width of the 2×RMS version of the galaxy NGC 4911

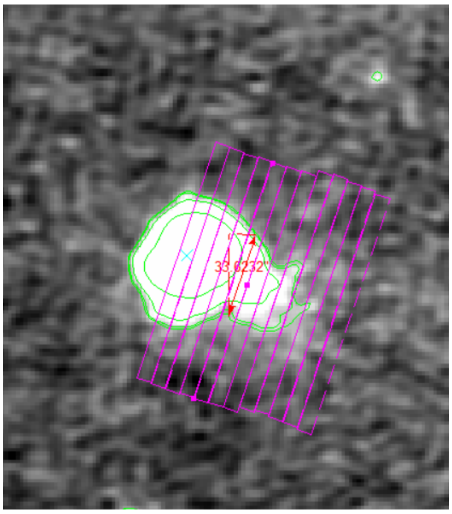

Figure 3.10: The process of measuring the tail width of the 4×RMS version of the galaxy NGC 4911

(see Figure 3.11and Figure 3.12). This function is defined by the parameter σ_{g}, which represents the standard deviation. To determine the FWHM, we must solve the equation where the function value is equal to half of the maximum amplitude

$$\exp\left(-\frac{(x-x_0)^2}{2\sigma_{\mathrm{g}}^2}\right) = 0.5 \tag{3.12}$$

After taking the logarithm, we obtain the constant 2.35482, allowing us to express the relationship as follows:

$$\mathrm{FWHM} = 2.35482 \cdot \sigma_{\mathrm{g}} \tag{3.13}$$

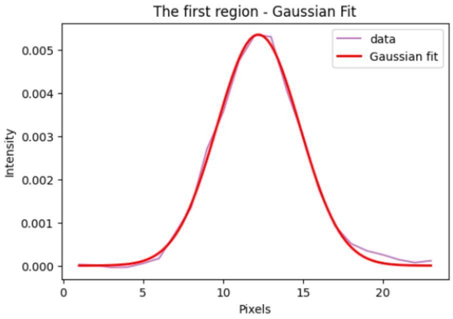

Figure 3.11: Gaussian fit for the first region over the disk of GMP 3779 galaxy (2×RMS)

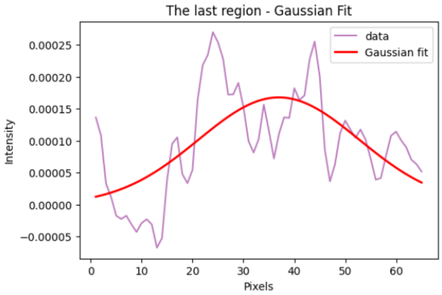

Figure 3.12: Gaussian fit for the last region over the tail of GMP 3779 galaxy (2×RMS)

As can be observed in Figure 3.11 and Figure 3.12, the Gaussian fit and the shape of the data profile differ significantly between the first and the last region which slice through the center of the disk, and the end of the tail, respectively. Therefore, when using this method, we excluded all FWHM values obtained from data that could not be properly fitted with a Gaussian function for each galaxy.

The second method utilized the *Ruler* tool, which was also employed for measuring the tail lengths. To maintain consistency, we used the previously defined regions as a guide (see Figure 3.9 and Figure 3.10). For each region, the ruler was stretched from the starting point of the outer contour to the corresponding point on the opposite side. The measured values for the individual galaxies for both variants (2×RMS and 4×RMS) are summarized in Table 4.2, Table 4.3, Table 4.4, Table 4.5, Table 4.6, Table 4.7 and Table 4.8 in Appendix.

The measurement of the apparent width of the emission within a 2×RMS contour is complementary to the first method as it effectively provides an isophotal width of the emission (or the width of the region where the intensity exceeds 2×RMS). If the profile is Gaussian, there is a clear relationship between the isophotal width and the FWHM, but if it is not Gaussian (showing multiple subpeaks and asymmetries as seen in Figure 3.12), it is not a direct proxy for FWHM.

The measured widths were not deconvolved from the synthesized beam, since our primary goal was to compare relative variations of the tail width along the emission rather than derive intrinsic physical widths, and because beam effects remain approximately constant across all measurements.

The final task was to plot our calculated and measured values for each galaxy. We created graphs showing how the galaxy width changes with increasing distance from the galactic center. The axes represent the distance from the center D_{cen} in arcseconds; since each individual region was 6 arcseconds wide, the distance was calculated in multiples of this value. The y-axis represents the width d_{gal} in arcseconds obtained through calculations

$$d_{\mathrm{gal}} = \mathrm{FWHM} \cdot \frac{l_{\mathrm{reg}}}{N}, \tag{3.14}$$

where l_{reg} is the lenght of the region and N is the number of pixels.

Values measured by the *Ruler* tool were already in arcseconds. Interestingly, the FWHM values obtained via Gaussian fitting show an upward trend. This is caused by the gradual broadening of the data in the region profiles and the emergence of structures (see Figure 3.12) that are increasingly difficult to fit with a Gaussian function, which subsequently leads to an increase in the FWHM width. The values measured with the Ruler tool generally decrease with increasing distance from the galactic center and this is what we would naturally expected.

The different behavior of the two width measurements is a consequence of how the methods respond to declining surface brightness and changing tail morphology along the radio tail. The Gaussian FWHM method measures the width of the bright central component, while the isophotal width measured above a fixed rms threshold depends strongly on the detectability of low-surface-brightness emission.

The first graph Figure 3.13 shows the dependence for the galaxy NGC 4848. It can be observed that this galaxy possesses the longest tail among the seven selected jellyfish galaxies (see also Figure 3.2). For the 2×RMS version, determining the width precisely was more challenging; as seen in Figure 3.3 , the galaxy's morphology in this version is irregular, and no significant initial decrease in width is observed.

The values remain within the range of 30–40 arcsec until reaching a distance of approximately 80 arcsec from the center. In contrast, the second version (4×RMS) shows a gradual decrease from the very beginning. The values of FWHM initially overlap for both versions of the galaxy images at the beginning.

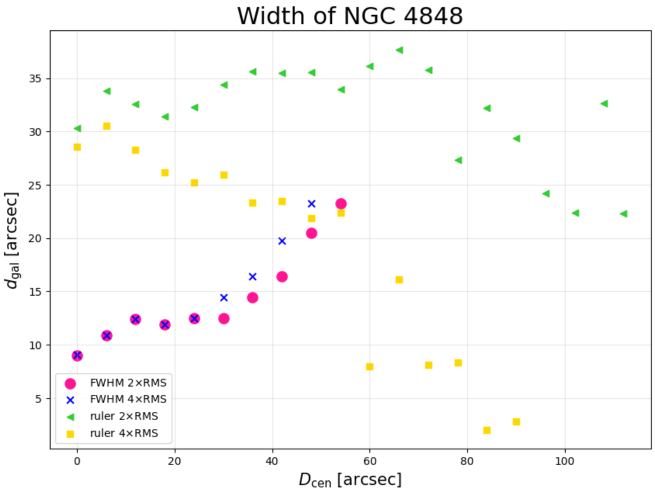

Figure 3.13: Width of 144 MHz radio emission in NGC 4848 as a function of distance from the galaxy center to the end of the tail.

In the case of galaxy IC 4040 in Figure 3.14, detection was achieved in only one version. Here, too, the results of our two methods differ. While the values obtained using the *Ruler* tool decrease, the FWHM values show an increase.

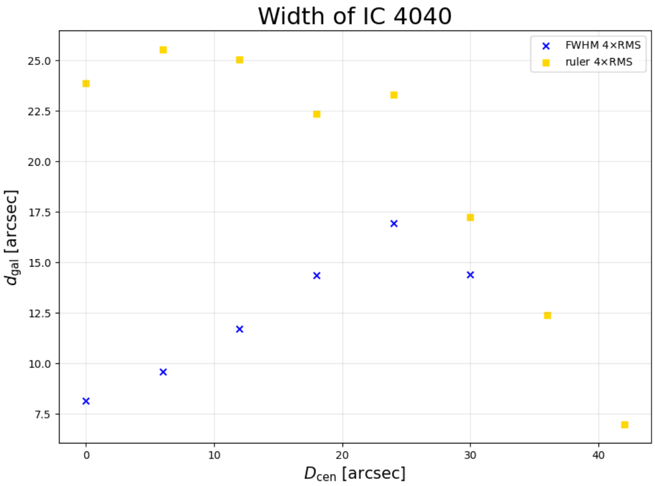

Figure 3.14: Width of 144 MHz radio emission in IC 4040 as a function of distance from the galaxy center to the end of the tail.

Galaxy IC 3949 is among those with a shorter tail, which resulted in fewer data points for our width measurements Figure 3.15. The FWHM method again shows an overlap between both versions and an upward trend. Regarding the Ruler method, the values fluctuate but remain within the range of 20 to 30 arcsec for the 2×RMS version. In the 4×RMS version, the galaxy is significantly shorter, and its width decreases with increasing distance from the center.

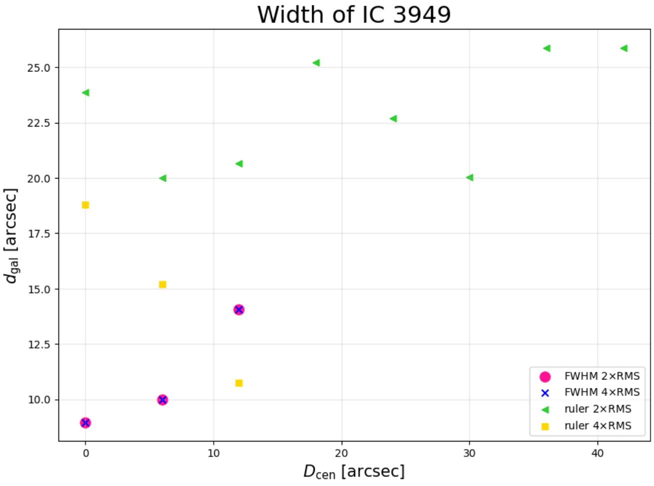

Figure 3.15: Width of 144 MHz radio emission in IC 3949 as a function of distance from the galaxy center to the end of the tail.

The following graph (Figure 3.16) illustrates how the width of galaxy GMP 3779 changes. Regarding the values measured with the *Ruler* tool, we again observe a decrease in both versions. For the FWHM data, the width remains approximately constant and maintains the same value in both versions.

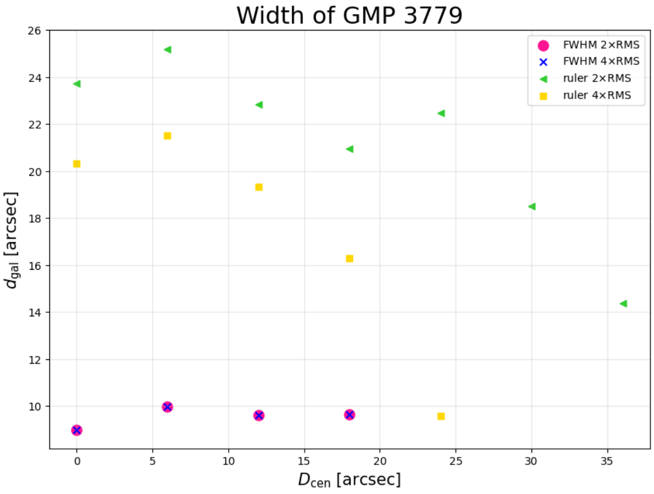

Figure 3.16: Width of 144 MHz radio emission in GMP 3779 as a function of distance from the galaxy center to the end of the tail.

For the galaxy NGC 4911, the values obtained using the FWHM method initially exhibit linear behavior, but then decrease before returning approximately to their previous levels in both versions. The values obtained with the Ruler tool gradually decrease, although slight fluctuations are again visible in the 2×RMS version (Figure 3.17).

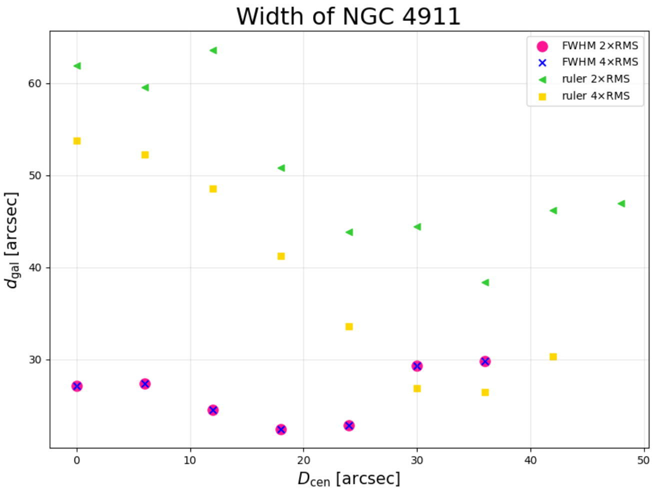

Figure 3.17: Width of 144 MHz radio emission in NGC 4911 as a function of distance from the galaxy center to the end of the tail.

In the case of NGC 4858 (Figure 3.18), the values measured with the *Ruler* tool for the 2×RMS version fluctuate extremely, as the tail of this galaxy is highly irregular in this version. In the 4×RMS version, the width decreases more steadily with increasing distance. The values obtained using the FWHM method again overlap for both versions and show a slight upward trend. For the 2×RMS version, we were unable to fit the data with a Gaussian function despite its Gaussian-like shape; therefore, these points are missing from the graph.

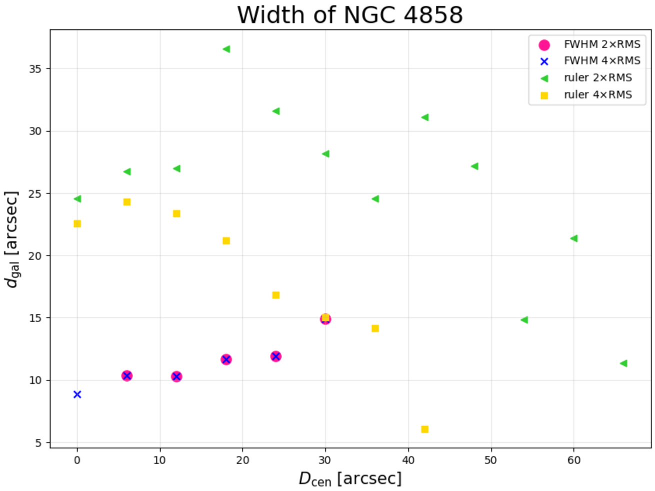

Figure 3.18: Width of 144 MHz radio emission in NGC 4858 as a function of distance from the galaxy center to the end of the tail.

For the final galaxy, GMP 4555 in Figure 3.19 the Ruler method in the 2×RMS version initially shows an approximately constant width, followed by a sharp decrease before stabilizing again. In contrast, the 4×RMS version exhibits a linear decrease in width with increasing distance. The FWHM values for both versions show a slight linear upward trend.

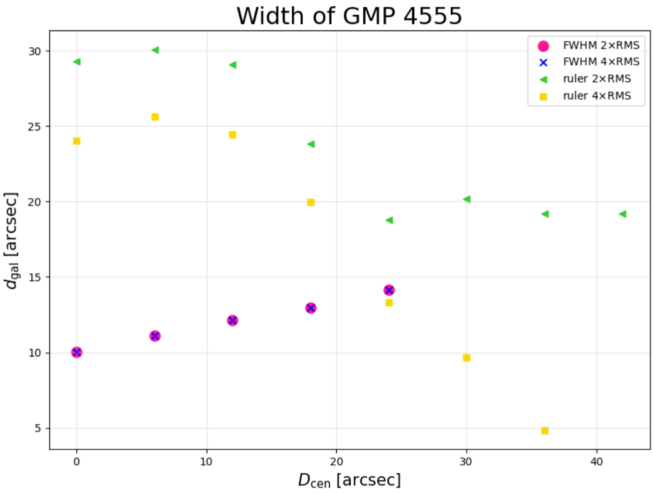

Figure 3.19: Width of 144 MHz radio emission in GMP 4555 as a function of distance from the galaxy center to the end of the tail.

The increasing FWHM width when moving farther from the galaxy likely corresponds to the combined effects of synchrotron losses, diffusion of cosmic rays, turbulence, and beam smearing. These effect tend to flatten and broaden the radio intensity distribution. The peak surface brightness decreases, while the emission becomes more diffuse, causing the fitted Gaussian profile to become wider and therefore producing an increasing FWHM with distance along the tail. In contrast, the measured isophotal width can remain constant or even decrease as the tail fades farther from the galaxy - its outer diffuse regions fall below the detection threshold, leaving only the brighter inner part detectable. We note that tails with approximately constant FWHM widths may indicate more efficient confinement of the relativistic plasma, for example by ordered magnetic fields, external intracluster-medium pressure, or a relatively steady stripping flow. However, projection effects can also play a major role. The observed width strongly depends on the angle between the tail and the line of sight, as well as on the orientation of the galactic disk relative to the ram-pressure wind.

Chapter 4

Comparison with Hα data

After measuring the radio continuum flux densities and tail lengths of the sample galaxies, we compared the results with the properties of the galaxies observed in Hα emission. Hα observations of jellyfish galaxies are an important tool for tracing the distribution of the warm ionized medium, identifying regions of ongoing star formation, and revealing gas ionized by shocks generated during ram-pressure interactions with the intracluster medium. The galaxy sample in the ALMA JELLY project was originally selected based on the presence of prominent Hα tails. The Hα observations were primarily taken from (Yagi et al. 2010), while data for galaxies GMP 4629, GMP 4570, and GMP 4555 were obtained from (Gavazzi et al. 2018), and observations of NGC 4848 were taken from (Fossati et al. 2012). These Hα data provide sufficiently high spatial resolution to reveal the morphology of compressed ionized gas and discrete star-forming knots within the stripped galactic tails. Measurements of the warm ionized gas tail lengths and Hα fluxes were compiled from the above-mentioned studies and are summarized in Table 4.1.

4.1 Comparing integrated flux densities

It is of particular interest to compare the integrated radio continuum flux densities of the sample galaxies with their total Hα fluxes measured within a fixed isophotal threshold (see (Yagi et al. 2010) for details). The flux values for the LOFAR observations from Table 3.2 and the corresponding Hα fluxes from Table 4.1 are shown in Figure 4.1. Upper limits are represented by open symbols. To improve the visualization and better capture the range of values, the axes were scaled logarithmically. As can be observed, the two quantities exhibit an overall positive correlation that can be reasonably described by a linear fit, although several galaxies deviate significantly from the general trend; therefore, we have labeled them individually for clarity.

This comparison is valuable because both radio continuum and Hα emission are closely linked to recent star formation activity, although they trace different physical components and timescales of the stellar population. Hα emission originates from ionized gas surrounding short-lived massive OB stars and therefore traces very recent star formation on timescales of a few Myr. In contrast, the radio continuum emission at 144 MHz is dominated by synchrotron radiation from cosmic-ray electrons accelerated in supernova remnants, tracing star formation over longer timescales of tens to hundreds of Myr.

Table 4.1: Parameters of jellyfish galaxies in Hα field

Name	l_{tail} [kpc]	Hα flux [erg s^{-1} cm^{-2}]
GMP 2910	60	$1.9 \cdot 10^{-14}$
NGC 4848	65	$4.0 \cdot 10^{-14}$
GMP 4060	81	$1.2 \cdot 10^{-15}$
IC 4040	90	$1.1 \cdot 10^{-13}$
IC 3949	34	$1.4 \cdot 10^{-16}$
GMP 3779	47	$3.7 \cdot 10^{-14}$
GMP 3071	35	$1.5 \cdot 10^{-15}$
GMP 4232	22	$1.0 \cdot 10^{-15}$
NGC 4911	28	$2.3 \cdot 10^{-13}$
GMP 2923	54	$6.6 \cdot 10^{-16}$
GMP 3016	34	$1.4 \cdot 10^{-16}$
GMP 3271	4.7	$1.4 \cdot 10^{-14}$
NGC 4858	21	$1.0 \cdot 10^{-13}$
NGC 4853	15	$6.4 \cdot 10^{-16}$
GMP 4629	10	$5.3 \cdot 10^{-15}$
GMP 4570	22	$3.4 \cdot 10^{-15}$
GMP 4555	24	$9.8 \cdot 10^{-15}$
NGC 4854	20	$2.4 \cdot 10^{-16}$

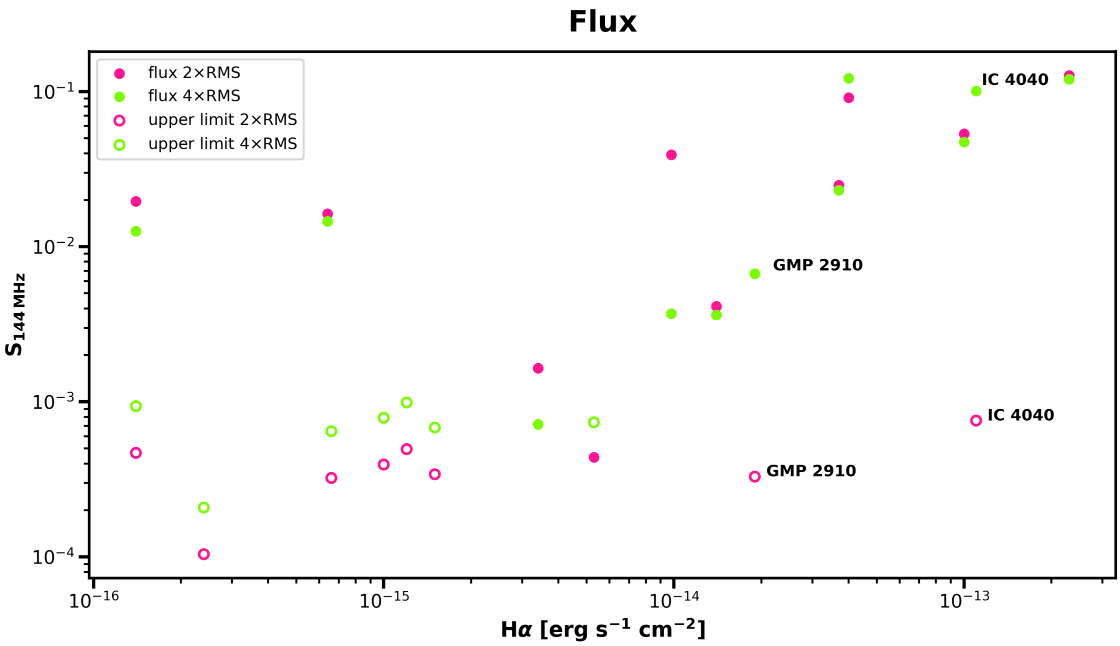

Figure 4.1: Hα flux versus 144 MHz flux density of the sample galaxies

For jellyfish galaxies, comparing these two tracers can reveal how ram-pressure stripping affects different phases of the interstellar medium and the propagation of cosmic rays into the stripped tails. For example, enhanced radio emission relative to Hα may indicate efficient transport or confinement of relativistic electrons and magnetic fields within the tail, while strong Hα emission without corresponding radio continuum emission may suggest very recent in-situ star formation or rapid synchrotron aging losses.

Qualitatively, the correlation in Figure 4.1 is related to the well-known correlation between radio luminosity and star formation rate observed in normal star-forming galaxies. Since Hα luminosity is commonly used as a star formation tracer, plotting radio continuum emission against Hα flux provides an approximate analogue to the standard 144 MHz luminosity–star formation rate relation.

A visual comparison between our data Figure 4.1 and the results Figure 4.2 published in (Roberts, Weeren, McGee, et al. 2021) reveals a high degree of consistency in the distribution of the observed objects. Our measurements (see Figure 4.1) exhibit similar linear trend, where an increase in radio intensity corresponds to a proportional increase in Hα emission. The correlation observed in our sample closely follows the trend established for jellyfish galaxies in the cited literature. Fundamentally, both plots represent the same physical principle, even though the axes are expressed through different parameters.

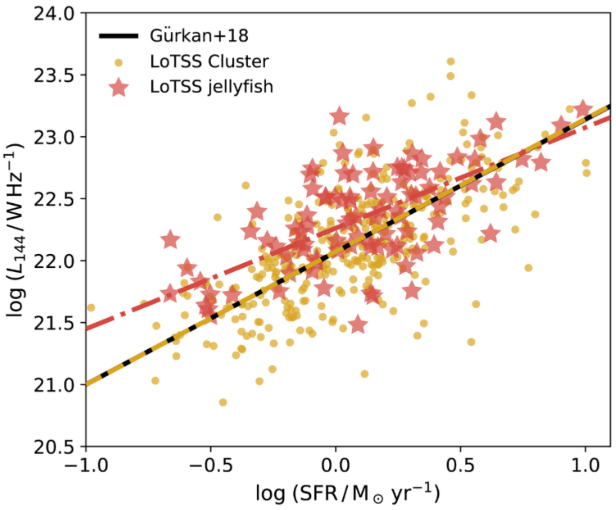

Figure 4.2: 144 MHz luminosity versus star formation rate (adopted from Roberts et al. (2021))

4.2 Comparing tail length

In the following Figure 4.4, the tail length values in the radio emission are plotted against the Hα emission (Table 4.1). We can observe that in most cases, there is no significant difference between the tail lengths in the two versions (2×RMS and 4×RMS). The largest discrepancy is found in the galaxy NGC 4848, where the difference reaches 44 kpc. When comparing the selected galaxies in the radio and Hα emission, we can see that the tail lengths do not differ substantially here either, with only a few exceptions such as IC 4040, where the difference amounts to 68 kpc or 2×RMS galaxy GMP 3779 where the difference is 37 kpc. For illustration, two selected galaxies with their Hα tails can be seen in Figure 4.3 – the images are adopted from (Yagi et al. 2010), where the galaxies are described in detail. We note that the discrepancy in tail length in the case of the galaxy IC 4040 corresponds to the complicated morphology of the Hα emission in this galaxy, which extends farther to the south, and is likely related to a past tidal interaction of the galaxy. With LOFAR, only the tail extending south-east from the disk is visible, whose Hα length is substantially shorter, about 42 kpc.

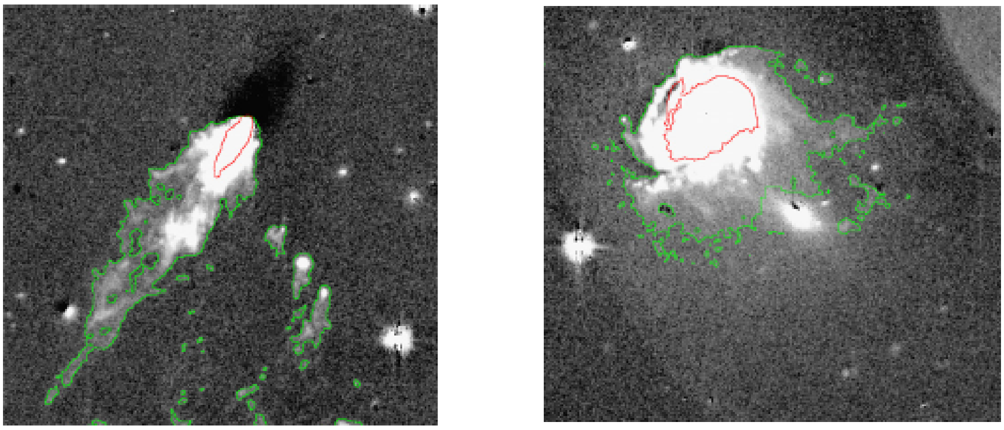

Figure 4.3: Galaxies IC 4040 and NGC 4911 in Hα emission (from Yagi et al. 2010)

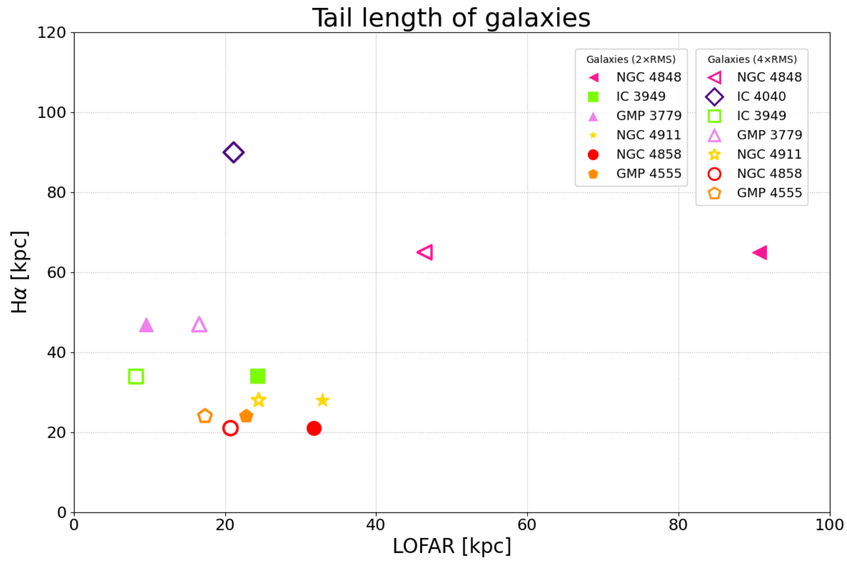

Figure 4.4: Graph of the length of the galaxy tails detected in radio cotinuum and Hα emission

Conclusions

In this bachelor's thesis, we investigated the properties of the radio continuum emission in a sample of 18 jellyfish galaxies in the Coma galaxy cluster. These galaxies are affected by the ram pressure exerted by the hot intracluster medium. The radio continuum emission corresponds primarily to synchrotron radiation produced by relativistic cosmic-ray electrons, which are generated in galaxies mainly during supernova explosions. Under the influence of ram pressure, these particles, together with the interstellar gas and magnetic fields, are removed from the galaxies and form characteristic "cometary" tails behind them. Specifically, we processed and analyzed radio continuum data at 144 MHz from the LoTSS project obtained with the LOFAR observatory and conducted a detailed examination of the morphology and geometry of selected detected galaxies.

In the first chapter, we introduced the observational background in Electromagnetic spectrum and the LOFAR - Low Frequency Array Observatory . The second chapter explores the mechanisms behind the formation of Jelyfish galaxies, focusing on Ram pressure stripping and the environmental conditions of the Coma cluster. In the third chapter (Data analysis), we described the procedures, analysis, and results of our measurements. The fourth chapter compares the results with the properties of the warm ionized gas component of the tails known from previous works.

From the LoTSS mosaic image covering the whole Coma cluster Figure 3.1, we first created cutouts of the images for individual galaxies, onto which we overlaid contours based on the robust estimate of the local noise level using a method of sigma clipping (Section 3.4.1). This is a crucial step since the sensitivity of the mosaic is far from uniform across the image. We found radio continuum is detected in 12 out of 18 galaxies. By defining the galaxy boundaries through multiples of the RMS noise, we were able to investigate their physical parameters, morphology and geometry. We measured the integrated flux density (or estimated upper limits) for the sample. These values were then shown in a graph (Figure 4.1) as a function of the corresponding Hα flux obtained for the sample jellyfish galaxies from the literature. The resulting plot clearly exhibits a positive linear correlation which qualitatively corresponds to the well known correlation between radio luminosity and star formation rate observed in normal star-forming galaxies.

Another investigated parameter was the projected tail length (Section 3.6.2), which we measured as the extent of the region where the intensity exceeds 2×RMS (or 4×RMS) level using the *Ruler* tool in the SAOImage DS9 software. These values were subsequently plotted in a graph in (Figure 4.4) as a function of the corresponding Hα tail lengths, allowing us to compare the similarities and differences between the tail lengths of the non-thermal radio continuum component and the warm ionized component traced by the Hα emission.

Our final task was to determine the projected width of the selected galaxies as a function of distance from the galactic center (Section 3.6.3). This measurement was performed using two methods: (1) measuring the FWHM of the Gaussian fit to the intensity profile along directions perpendicular to the tail, and (2) measuring the isophotal width of the tail along the same perpendicular directions. The DS9 tools *Ruler* and *Projection* were used. Through this analysis, we found that the former method mostly revealed increasing widths of the tails when moving farther from the galaxy, which may correspond to the combined effects of synchrotron losses, diffusion of cosmic rays, turbulence, and beam smearing. A few tails showed approximately constant FWHM widths which may indicate more efficient confinement of the stripped relativistic plasma.

Appendix

Table 4.2: Values of FWHM and ruler measured width of galaxy NGC 4848

FWHM (2×RMS) [arcsec]	FWHM (4×RMS) [arcsec]	Ruler (2×RMS) [arcsec]	Ruler (4×RMS) [arcsec]
6.027	6.061	30.334	28.601
7.278	7.278	33.802	30.512
8.323	8.323	32.546	28.300
7.962	7.962	31.414	26.145
8.349	8.349	32.247	25.187
8.349	9.674	34.402	25.965
9.674	11.025	35.658	23.334
11.025	13.266	35.482	23.453
13.735	15.608	35.538	21.897
15.606	15.851	33.925	22.375
15.851		36.136	7.963
		37.692	16.096
		35.784	8.135
		27.346	8.321
		32.193	2.034
		29.380	2.809
		24.232	2.717
		22.376	
		32.630	
		22.329	

Table 4.3: Values of FWHM and ruler measured width of galaxy IC 4040

FWHM (4×RMS) [arcsec]	Ruler 4×RMS) [arcsec]
5.532	23.864
6.500	25.551
7.945	25.061
9.759	22.337
11.495	23.318
9.783	17.235
	12.373
	6.977

Table 4.4: Values of FWHM and ruler measured width of galaxy IC 3949

FWHM (2×RMS) [arcsec]	FWHM (4×RMS) [arcsec]	Ruler (2×RMS) [arcsec]	Ruler (4×RMS) [arcsec]
6.132	6.132	23.848	18.786
6.837	6.837	19.987	15.187
9.610	9.610	20.669	10.749
		25.208	
		22.683	
		20.024	
		25.879	
		25.880	

Table 4.5: Values of FWHM and ruler measured width of galaxy GMP 3779

FWHM (2×RMS) [arcsec]	FWHM (4×RMS) [arcsec]	Ruler (2×RMS) [arcsec]	Ruler (4×RMS) [arcsec]
6.075	6.075	23.743	20.325
6.729	6.729	25.196	21.498
6.486	6.486	22.841	19.338
6.510	6.510	20.952	16.275
12		22.480	9.5734
		18.513	11.466
		14.357	

Table 4.6: Values of FWHM and ruler measured width of galaxy NGC 4911

FWHM (2×RMS) [arcsec]	FWHM (4×RMS) [arcsec]	Ruler (2×RMS) [arcsec]	Ruler (4×RMS) [arcsec]
18.096	18.096	61.895	53.778
18.299	18.299	59.5849	52.234
16.395	16.395	63.6244	48.558
15.001	15.000	50.8479	41.255
15.236	15.235	43.164	33.623
19.595	19.595	44.4254	26.886
19.924	19.924	38.398	26.434
		46.199	30.338
		46.965	

Table 4.7: Values of FWHM and ruler measured width of galaxy NGC 4858

FWHM (2×RMS) [arcsec]	FWHM (4×RMS) [arcsec]	Ruler (2×RMS) [arcsec]	Ruler (4×RMS) [arcsec]
-	5.957	24.588	22.594
6.987	6.987	26.758	24.285
6.916	6.916	26.960	23.359
7.872	7.872	36.610	21.189
8.026	8.026	31.627	16.802
10.056	10.056	28.169	15.038
		24.545	14.126
		31.123	6.076
		27.202	
		14.828	
		21.368	
		11.359	

Table 4.8: Values of FWHM and ruler measured width of galaxy GMP 4555

FWHM (2×RMS) [arcsec]	FWHM (4×RMS) [arcsec]	Ruler (2×RMS) [arcsec]	Ruler (4×RMS) [arcsec]
6.741	6.741	29.273	24.025
7.466	7.466	30.081	25.639
8.150	8.150	29.072	24.428
8.707	8.707	23.823	19.990
9.500	9.500	18.776	13.330
		20.188	9.692
		19.180	4.849
		19.180	

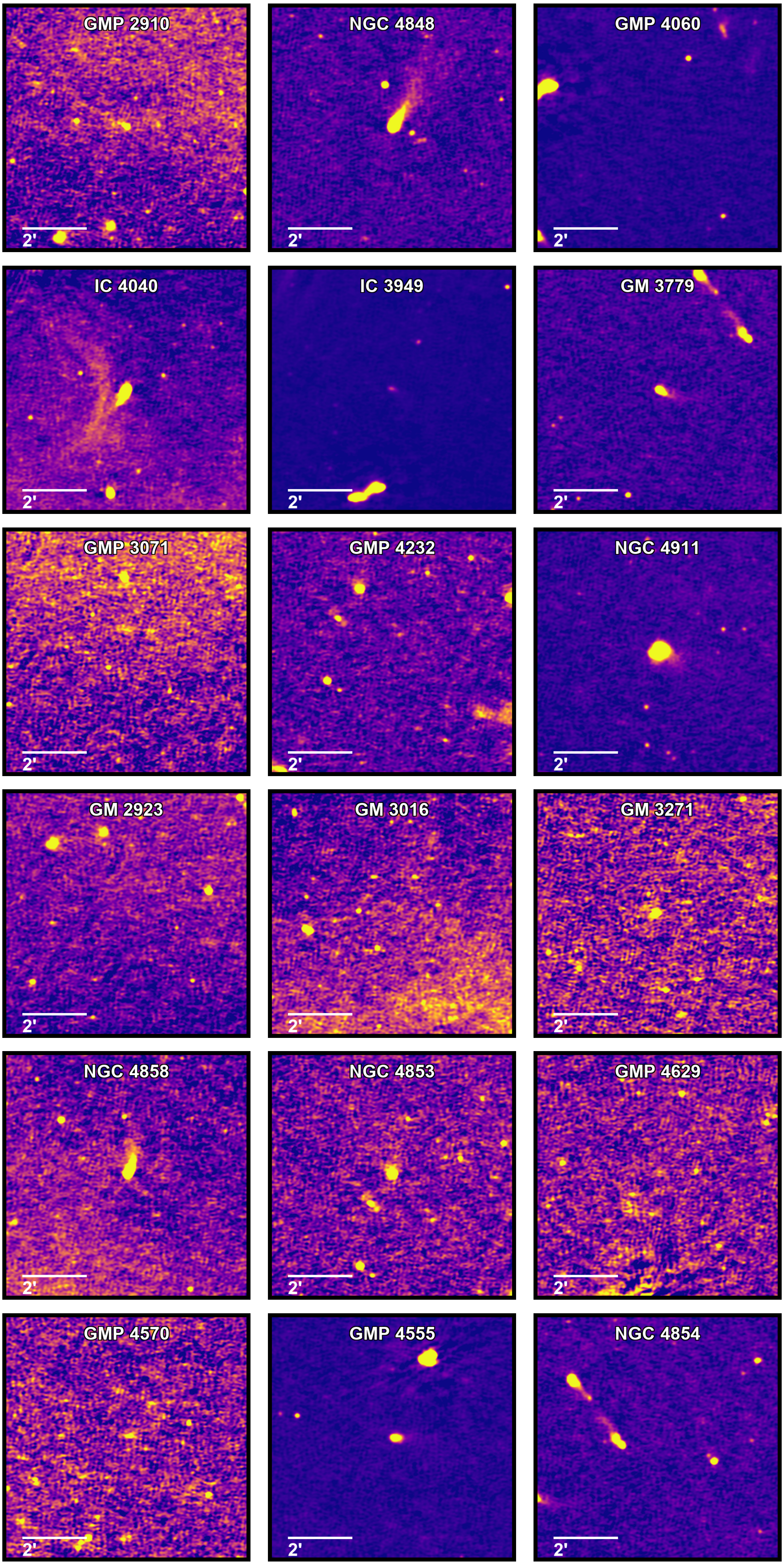

Figure 4.5: Overview of galaxies cut out from the composite LOFAR image

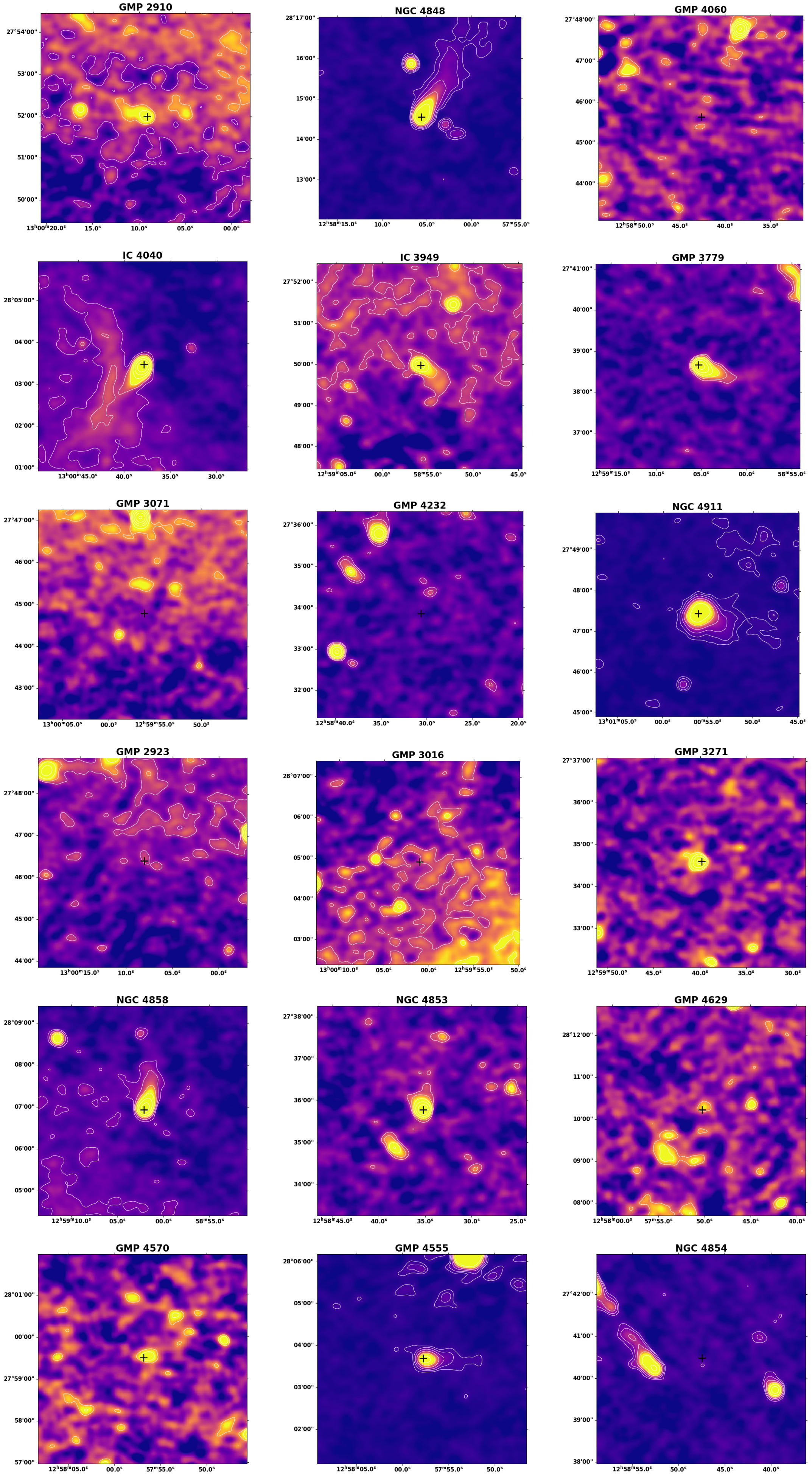

Figure 4.6: Overview of galaxies with rendered contours for the 2× RMS smoothed version

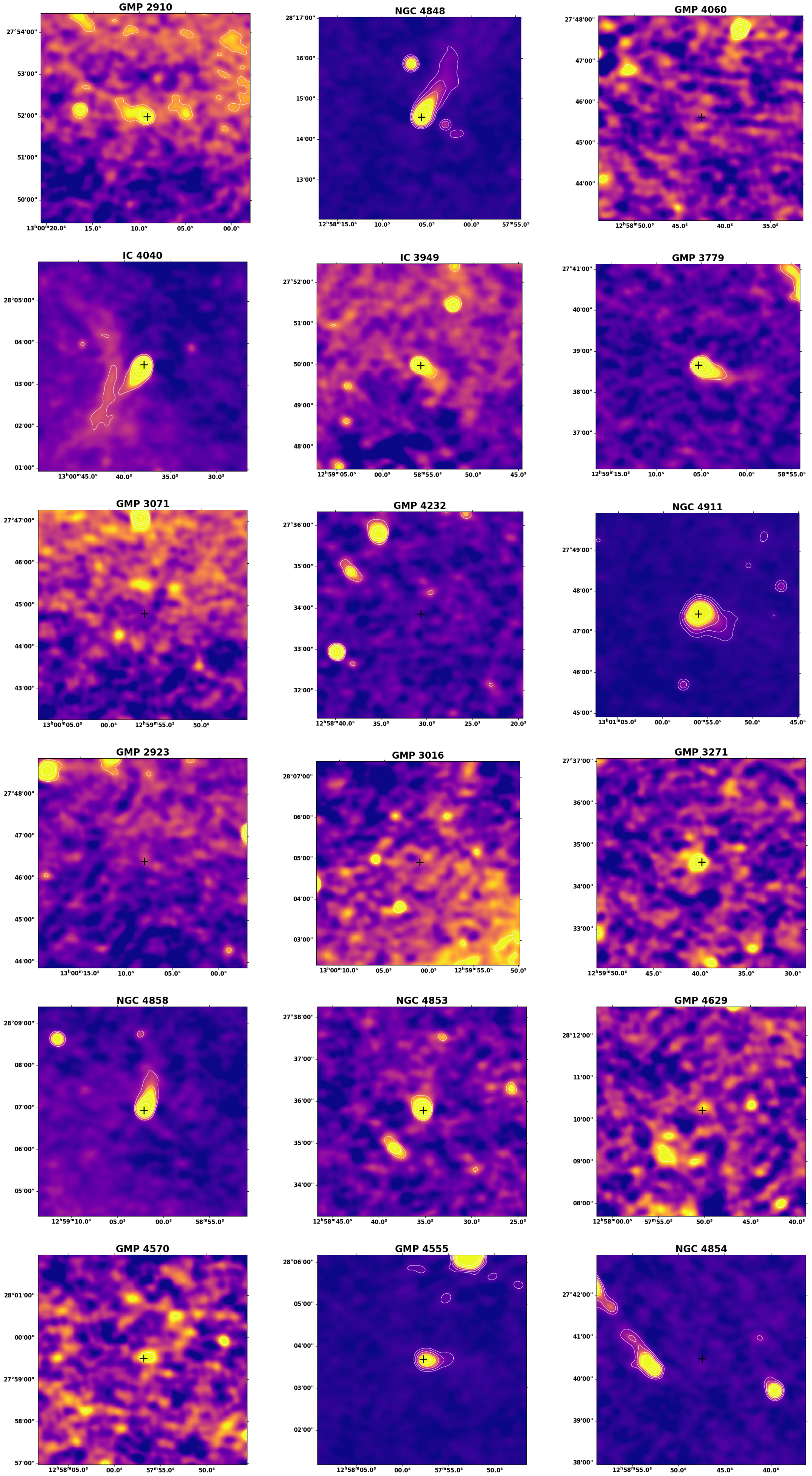

Figure 4.7: Overview of galaxies with rendered contours for the 4× RMS smoothed version

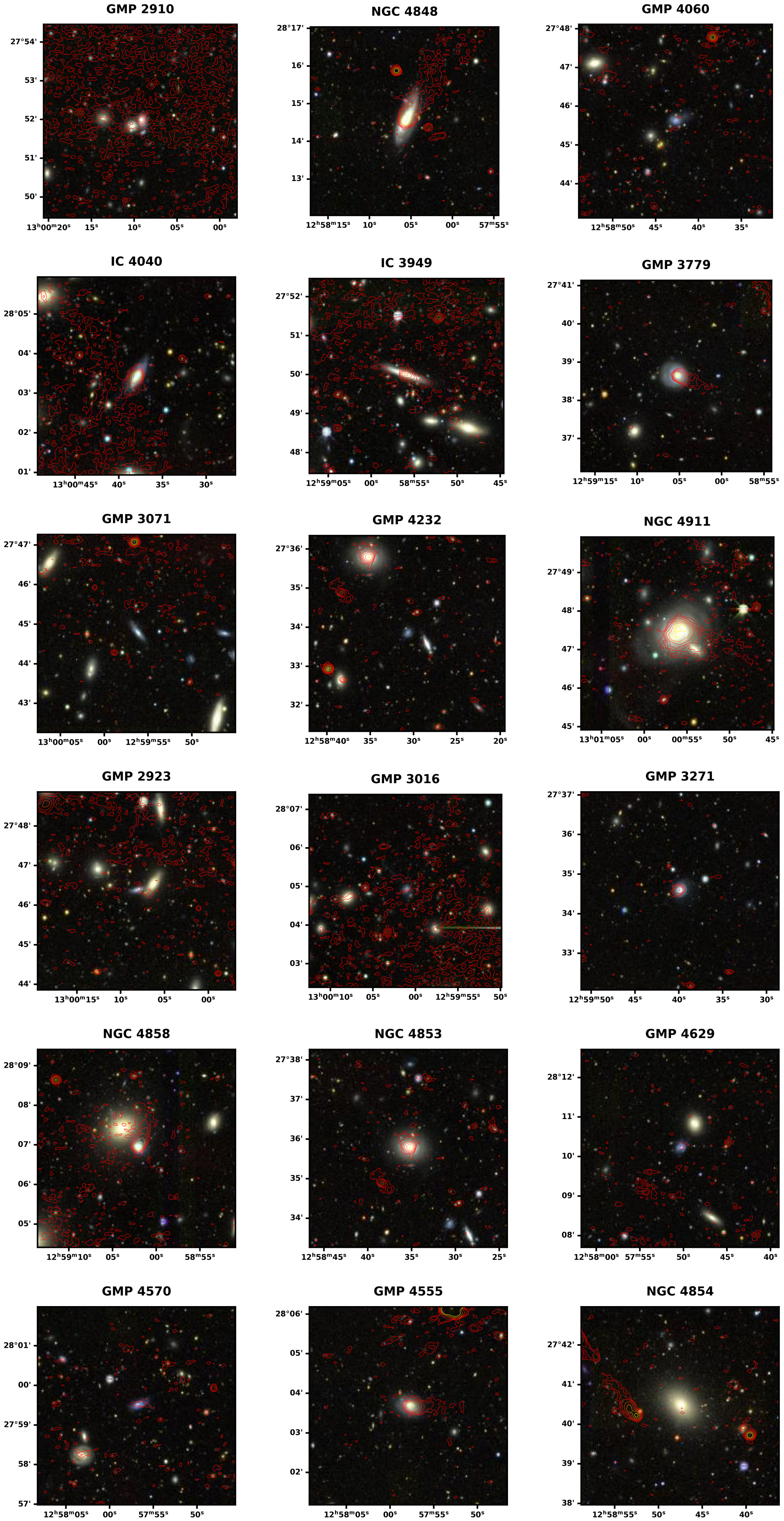

Figure 4.8: Galaxy images in visible field with 2×RMS contours

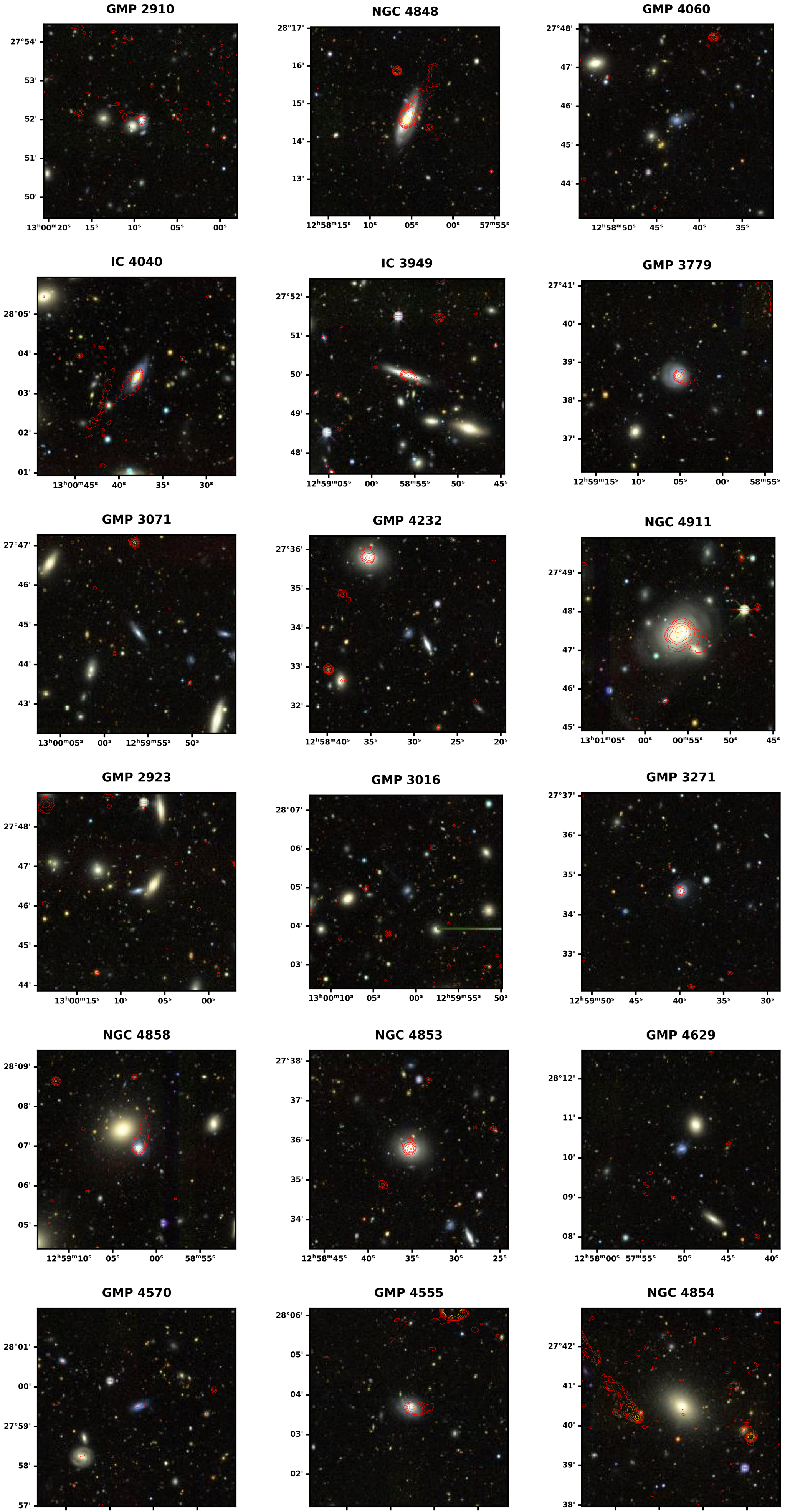
GMP 2910

NGC 4848

GMP 4060

IC 4040

IC 3949

GMP 3779

GMP 3071

GMP 4232

NGC 4911

GMP 2923

GMP 3016

GMP 3271

NGC 4858

NGC 4853

GMP 4629

GMP 4570

GMP 4555

NGC 4854

Figure 4.9: Galaxy images in visible field with 4×RMS contours

Bibliography

Boselli, Alessandro, Matteo Fossati, and Ming Sun (Dec. 2022). “Ram pressure stripping in high-density environments”. In: 30.1, 3, p. 3. DOI: 10.1007/s00159-022-00140-3. arXiv: 2109.13614 [astro-ph.GA].

Cowie, L. L. and A. Songaila (Apr. 1977). “Thermal evaporation of gas within galaxies by a hot intergalactic medium”. In: 266, pp. 501–503. DOI: 10.1038/266501a0.

Dey, Arjun et al. (Apr. 2019). “Overview of the DESI Legacy Imaging Surveys”. In: *The Astronomical Journal* 157.5, p. 168. ISSN: 1538-3881. DOI: 10.3847/1538-3881/ab089d. URL: http://dx.doi.org/10.3847/1538-3881/ab089d.

Fossati, Matteo et al. (Aug. 2012). “65 kpc of ionized gas trailing behind NGC 4848 during its first crossing of the Coma cluster”. In: *A&A* 544, A128, A128. DOI: 10.1051/0004-6361/201219933. arXiv: 1207.4806 [astro-ph.CO].

Gavazzi, G. et al. (Oct. 2018). “Ubiquitous ram pressure stripping in the Coma cluster of galaxies”. In: *A&A* 618, A130, A130. DOI: 10.1051/0004-6361/201833427. arXiv: 1808.04575 [astro-ph.GA].

Gunn, James E. and J. Richard Gott III (Aug. 1972). “On the Infall of Matter Into Clusters of Galaxies and Some Effects on Their Evolution”. In: *ApJ* 176, p. 1. DOI: 10.1086/151605.

Haarlem, M. P. van et al. (2013). “LOFAR: The LOw-Frequency ARray”. In: *Astronomy amp; Astrophysics* 556, A2. ISSN: 1432-0746. DOI: 10.1051/0004-6361/201220873. URL: http://dx.doi.org/10.1051/0004-6361/201220873.

Lee, Seona et al. (Dec. 2022). “Ram pressure stripping and ISM disc truncation: prediction versus observation”. In: *MNRAS* 517.2, pp. 2912–2924. DOI: 10.1093/mnras/stac2821. arXiv: 2209.15235 [astro-ph.GA].

Malavasi, Nicola et al. (Jan. 2020). “Like a spider in its web: a study of the large-scale structure around the Coma cluster”. In: *Astronomy amp; Astrophysics* 634, A30. ISSN: 1432-0746. DOI: 10.1051/0004-6361/201936629. URL: http://dx.doi.org/10.1051/0004-6361/201936629.

Roberts, I. D., R. J. van Weeren, D. V. Lal, et al. (2023). *Radio-continuum spectra of ram pressure stripped galaxies in the Coma Cluster*. arXiv: `2310.20417 [astro-ph.GA]`. URL: `https://arxiv.org/abs/2310.20417`.

Roberts, I. D., R. J. van Weeren, S. L. McGee, et al. (2021). "LoTSS jellyfish galaxies: I. Radio tails in low redshift clusters". In: *Astronomy amp; Astrophysics* 650, A111. ISSN: 1432-0746. DOI: `10.1051/0004-6361/202140784`. URL: `http://dx.doi.org/10.1051/0004-6361/202140784`.

Shimwell, T. W., M. J. Hardcastle, C. Tasse, P. N. Best, et al. (Mar. 2022). "The LOFAR Two-metre Sky Survey. V. Second data release". In: *A&A* 659, A1, A1. DOI: `10.1051/0004-6361/202142484`. arXiv: `2202.11733 [astro-ph.GA]`.

Shimwell, T. W., M. J. Hardcastle, C. Tasse, A. Drabent, et al. (Mar. 2026). "The LOFAR Two-metre Sky Survey: VII. Third Data Release". In: *A&A* 707, A198, A198. DOI: `10.1051/0004-6361/202557749`. arXiv: `2602.15949 [astro-ph.GA]`.

Shimwell, T. W., H. J. A. Röttgering, et al. (Feb. 2017). "The LOFAR Two-metre Sky Survey: I. Survey description and preliminary data release". In: *Astronomy amp; Astrophysics* 598, A104. ISSN: 1432-0746. DOI: `10.1051/0004-6361/201629313`. URL: `http://dx.doi.org/10.1051/0004-6361/201629313`.

Shimwell, T. W., C. Tasse, et al. (Feb. 2019). "The LOFAR Two-metre Sky Survey: II. First data release". In: *Astronomy amp; Astrophysics* 622, A1. ISSN: 1432-0746. DOI: `10.1051/0004-6361/201833559`. URL: `http://dx.doi.org/10.1051/0004-6361/201833559`.

Yagi, Masafumi et al. (Dec. 2010). "A Dozen New Galaxies Caught in the Act: Gas Stripping and Extended Emission Line Regions in the Coma Cluster". In: *AJ* 140.6, pp. 1814–1829. DOI: `10.1088/0004-6256/140/6/1814`. arXiv: `1005.3874 [astro-ph.CO]`.